CHALMERS
UNIVERSITY OF TECHNOLOGY

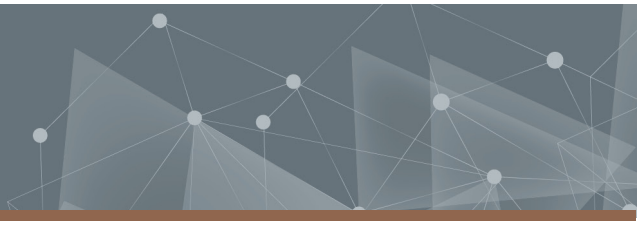

Characterizing Thermal Populations in a Coupled Superconducting Aluminum 3D-cavity and a Transmon Qubit

Master's thesis in Physics

IVAN HAGSTRÖM

DEPARTMENT OF MICROTECHNOLOGY AND NANOSCIENCE

CHALMERS UNIVERSITY OF TECHNOLOGY
Gothenburg, Sweden 2023
www.chalmers.se

Master's thesis 2023

Characterizing Thermal Populations in a Coupled Superconducting Aluminum 3D-cavity and a Transmon Qubit

IVAN HAGSTRÖM

CHALMERS
UNIVERSITY OF TECHNOLOGY

Department of Microtechnology and Nanoscience
Division of Quantum Technology
202Q-LAB
Chalmers University of Technology
Gothenburg, Sweden 2023

Characterizing Thermal Populations in a Coupled Superconducting Aluminum 3D-cavity and a Transmon Qubit
IVAN HAGSTRÖM

Supervisor: Dr. Mikael Kervinen, Department of Microtechnology and Nanoscience
Co-supervisor: Marina Kudra, Department of Microtechnology and Nanoscience
Examiner: Prof. Simone Gasparinetti, Department of Microtechnology and Nanoscience

Master's Thesis 2023
Department of Microtechnology and Nanoscience
Division of Quantum Technology
202Q-LAB)
Chalmers University of Technology
SE-412 96 Gothenburg
Telephone +46 31 772 1000

Typeset in LaTeX
Printed by Chalmers Reproservice
Gothenburg, Sweden 2023

Characterizing Thermal Populations in a Coupled Superconducting Aluminum 3D-cavity and a Transmon Qubit

IVAN HAGSTRÖM
Department of Microtechnology and Nanoscience
Chalmers University of Technology

Abstract

Circuit quantum electrodynamics (cQED), which combines superconducting qubits with microwave resonators, has become one of the leading platforms for quantum computation [1]. Continuous variable quantum computation (CVQC), which uses the bosonic modes of a quantum microwave resonator as a quantum memory, has some advantages over discrete quantum computing, including long lifetimes and simple schemes for error correction [2]. The presence of thermal excitations in a continuous variable system can increase error rates and reduce the fidelity of quantum operations. This provides the motivation to characterize the residual thermal population of our systems. In this thesis we demonstrate methods for characterizing the residual thermal populations in a coupled superconducting 3D-cavity and transmon qubit. First, the qubit population was measured following the scheme from Geerlings et al. (2013) [3]. The measured population was $0.25 \pm 0.06\%$ corresponding to an effective temperature of 50.2 ± 1.9 mK. Second, two different methods were used to measure the thermal population of the 3D-cavity. One based on Rabi driving and one based on Ramsey interferometry. Of the two, the method using Rabi driving seemed to perform better at small populations in terms of standard deviation. With this method we measuring a residual population of $0.34 \pm 0.03\%$ corresponding to an effective temperature of 37.6 ± 0.3 mK. Finally, the thermal population of an on-chip readout resonator coupled to the qubit was estimated using the photon induced dephasing of the qubit. This gave a population of $< 0.18\%$ corresponding to an effective temperature of < 56.1 mK. These results compare favorable to previous studies such as J. M. Gertler et al. (2021) who measured a cavity population of 1-2% and a transmon population of 5% in a similar system [4], and R. W. Heeres et al. (2017) who measured a population of 2% in their cavity and 5% in their transmon [5]. An additional sub-goal of this thesis was measuring the quality factor of a niobium 3D-cavity. Using a circle fit [6], a quality factor of approximately 4.3 million was measured, which is an expected result for an unpolished cavity.

Keywords: 3D-cavity, Circuit quantum electrodynamics, Continuous variable quantum computing, qubit, thermal excitation, thermal population

Acknowledgements

I want to express my gratitude to Prof. Simone Gasparinetti, Dr. Mikael Kervinen and Marina Kudra for making this project possible. Having them as my examiner and supervisors has been a great pleasure. They have helped me a lot throughout and never hesitated to answer my questions and explain concepts I struggled with understanding. I would also like to thank the rest of the 202Q group for their support and all the great discussion they have provided. I am also grateful to my friend and opponent Alexei Orekhov for his insightful critique and feedback, as well as my proofreaders, including Núria Alcalde Herraiz and Emelie Nilsson. Finally, I would like to thank my friends and family for always supporting me and pushing me forward when I need it the most. I wouldn't have come this far without you.

Ivan Hagström, Gothenburg, December 2022

Contents

1
Introduction

Since its inception in the late 20th century, the field of quantum computation has studied ways to use the properties of a quantum system, such as parallelism and quantum interference, to gain an advantage over classical computing. Quantum algorithms have been proven theoretically useful for a number of different problems that classical computers have a hard time solving, or cannot solve all together [7], [8], [9]. One of the first such problems was the simulation of quantum systems. Due to the probabilistic nature of quantum mechanics, quantum systems cannot be simulated efficiently on a classical computer. In the year 1981, Richard P. Feynman suggested that we could instead use a quantum system to simulate other quantum systems [10]. Because the simulator would itself be inherently quantum in nature it would get around the problems of simulating quantum systems with classical computers. This universal quantum simulator would be called a quantum computer.

The prospect of using quantum computation to improve classical algorithms for information processing also showed great potential. One of the first algorithms to demonstrate an exponential speed-up as compared to its classical counterpart was the 1992 Deutsch-Jozsa algorithm [7]. The algorithm is used to survey a binary function to determine whether it is constant or balanced. While not of much practical use, it acted as a proof of concept for quantum speed-up. A few years later, Lov K. Grover suggested a quantum search algorithm for an unstructured database search, providing a polynomial speed-up compared to its classical counterparts [8]. Classically, the best we can do is pull random items until we find the one we are looking for. The Grover algorithm uses a technique called amplitude amplification to increase the probability of pulling the correct item to an arbitrary degree, providing a speed-up. During this time, Peter Shor also formulated his famous algorithm for prime number factorization, known as Shor's algorithm [9]. The algorithm is a complicated set of quantum operations, including the quantum Fourier transform, that exploit quantum interference to find the prime number factors of large integer numbers at exponential speed-up.

One of the greatest challenges for quantum computation is the physical realization of the basic quantum computational component, the qubit. Many physical platforms for implementing qubits have been experimentally demonstrated, such as electron spins in quantum dots [11], polarized photons [12] and trapped ions [13]. One of the most promising platforms, however, is the superconducting qubit, which exploits the properties of superconductivity to create an "artificial atom" that can be configured to fit the specific needs of the implementation [14]. Another advantage of supercon-

ducting qubits is that they are an on-chip technology like classical CPUs, and are compatible with existing fabrication techniques. There are many different types of superconducting qubits. The most widely used, due to its robustness against noise, is the transmon qubit [1].

Circuit quantum electrodynamics (cQED) studies the interaction between superconducting qubits and quantized electromagnetic fields, such as a qubit coupled to an on-chip resonator or a superconducting 3D-cavity [1]. The properties of this type of architecture can be exploited to perform quantum computation. Coupling a superconducting qubit to a resonator, the bosonic modes of the resonator can act as a quantum memory while the qubit provides the non-linearity needed for quantum computation. This form of quantum computing is usually called continuous variable quantum computation. The interaction between the qubit and an on-chip resonator can provide the means to perform readout of the qubit state while a superconducting 3D-cavity resonator is suitable for acting as quantum memory due to its high quality factor and long lifetime. Additionally, the cavity only has a single dominant decay channel making error correction relatively easy to implement. This can for example be done by encoding computational states in even quantum states. An error can then be detected by performing a parity measurement [2]. Furthermore, high-fidelity preparation of various useful quantum states in this type of architecture has been demonstrated [15].

For a quantum system to be used for quantum computation it needs to be sufficiently isolated from its warm environment that thermal noise does not cause the system to decohere and lose information. Heat flowing in from the environment causes thermal excitations in the quantum system. This residual thermal population in the system, caused by incoherent thermal excitations, can disrupt quantum operations and reduce the fidelity of quantum gates, state preparation, state readout, etc. This provides a strong motivation to develop methods for characterizing the thermal noise in a quantum system. Methods have been developed to measure the thermal excited-state population of a qubit for this purpose [3]. In the interest of being able to perform quantum computation with a continuous variable system, there is also a need for methods to measure the thermal populations of the coupled cavity and readout resonator of the system.

The aim of this project is to characterize thermal populations, ie. the population caused by thermal excitations, in a superconducting aluminum 3D-cavity and a transmon qubit coupled to each other. First, the thermal population of the qubit will be measured using the method presented in Geerlings et al. (2012) [3], which utilizes Rabi driving the e-f transition of the qubit to measure its excited state population. Second, two different methods will be used to measure the thermal population of the 3D-cavity. One is based on Rabi driving and was previously described in A. P. Sears (2012) [16]. The other is based on Ramsey interferometry. These two methods will then be benchmarked against each other. Lastly, the thermal population of the readout resonator will be estimated. While we cannot measure it directly due to it not being in the photon number resolved regime, we can find an upper bound for it

using the dephasing of the qubit.

In addition to the population measurements, a subgoal of this thesis is to characterize the quality factor of a niobium 3D-cavity, niobium being a good alternative to aluminum with potential to provide a higher quality factor [17].

2

Theoretical Background

In this section I explain the theoretical background that the project is built on. I start at the quantum harmonic oscillator which is derived from the classical LC resonator by quantizing it. I then introduce the Josephson junction and how it is used to create a transmon qubit. Following this I explain how these two components interact and how the qubit can be controlled through Rabi driving. Finally, I describe noise in our model and what causes it.

2.1 The Quantum Harmonic Oscillator

A classical one-dimensional electromagnetic mode can be modelled as an LC resonator (Figure 2.1) and characterized by its resonance frequency $\omega_c = \frac{1}{\sqrt{LC}}$ and impedance $Z_c = \sqrt{\frac{L}{C}}$, where L and C are the inductance and capacitance of the resonator [1].

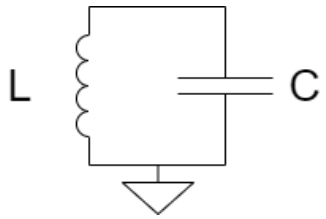

Figure 2.1: Circuit diagram for an LC resonator.

Its dynamics are described by its Hamiltonian:

$$H = \frac{Q^2}{2C} + \frac{\Phi^2}{2L}, \tag{2.1}$$

where the first term is the kinetic energy and the second term is the potential energy [1]. Analogous to the LC resonator the quantum harmonic oscillator Hamiltonian, ie. the quantum treatment of such a mode, can be written as

$$H = \frac{\hat{Q}^2}{2C} + \frac{\hat{\Phi}^2}{2L}, \tag{2.2}$$

where the total charge of the capacitor, $\hat{Q}$, and total magnetic flux through the loop, $\hat{\Phi}$, have been promoted to quantum operators with the commutation relation $[\hat{\Phi}, \hat{Q}] = i\hbar$ [1]. It is convenient now to introduce the non-unitary creation and annihilation operators, $\hat{a}$ and $\hat{a}^\dagger$, such that

$$\hat{Q} = iQ_{zpf}(\hat{a} - \hat{a}^\dagger), \tag{2.3a}$$

$$\hat{\Phi} = \Phi_{zpf}(\hat{a} + \hat{a}^\dagger), \tag{2.3b}$$

where $Q_{zpf} = \sqrt{\frac{\hbar\omega_c C}{2}}$ and $\Phi_{zpf} = \sqrt{\frac{\hbar}{2\omega_c C}}$ are the zero-point fluctuations of the charge and the flux, respectively [1]. Using the commutation relation of $\hat{Q}$ and $\hat{\Phi}$ it can

be shown that $\hat{a}$ and $\hat{a}^\dagger$ have the commutation relation $[\hat{a}, \hat{a}^\dagger] = 1$. With these new operators we can rewrite the quantum harmonic oscillator Hamiltonian as

$$H = \hbar\omega_c \left(\hat{a}^\dagger \hat{a} + \frac{1}{2}\right). \tag{2.4}$$

The operator $\hat{n} = \hat{a}^\dagger \hat{a}$ is called the number operator and denotes the number of excitations in our quantum harmonic oscillator, ie. the number of photons [18]. From the eigenvalue equation, $H|n\rangle = E_n|n\rangle$, we can find the eigenenergies of this Hamiltonian to be

$$E_n = \hbar\omega_c \left(n + \frac{1}{2}\right). \tag{2.5}$$

The energy potential and energy levels of the harmonic oscillator are plotted in Figure 2.6. The eigenstates $|n\rangle$ called Fock states or number states are orthonormal, $\langle n|m\rangle = \delta_{nm}$, and thus form a complete basis for the quantum harmonic oscillator. This means that any state it can take can be expressed as a sum of Fock states, $|\psi\rangle = \sum_n c_n |n\rangle$ [18]. It can also be shown that the Fock states follow the relations

$$\hat{a}|n\rangle = \sqrt{n}\,|n-1\rangle, \tag{2.6a}$$

$$\hat{a}^\dagger|n\rangle = \sqrt{n+1}\,|n+1\rangle, \tag{2.6b}$$

$$\hat{a}^\dagger\hat{a}|n\rangle = n|n\rangle. \tag{2.6c}$$

The ground state of the harmonic oscillator, $|0\rangle$ with energy $\frac{1}{2}\hbar\omega_c$, is usually called the vacuum state [18].

Another state that will become relevant in this project is the coherent state $|\alpha\rangle$, defined by $\hat{a}|\alpha\rangle = \alpha|\alpha\rangle$ [18]. Rewriting this in terms of the Fock states we can see that the coherent state must take the form

$$|\alpha\rangle = e^{-|\alpha|^2/2} \sum_n \frac{\alpha^n}{\sqrt{n!}} |n\rangle, \tag{2.7}$$

$$P_n = e^{-|\alpha|^2} \frac{|\alpha|^{2n}}{n!} = e^{-\bar{n}} \frac{\bar{n}^n}{n!}. \tag{2.8}$$

Coherent states have a Poissonian photon distribution with the average photon number $\langle\alpha|\hat{a}^\dagger\hat{a}|\alpha\rangle = |\alpha|^2 \equiv \bar{n}$ [18]. Importantly, $\langle\beta|\alpha\rangle = e^{-\frac{1}{2}(|\beta|^2+|\alpha|^2-2\beta^*\alpha)} \neq 0$ for $\beta \neq \alpha$, which means that coherent states are not orthogonal and therefore not perfectly distinguishable from each other, except in the limit $|\alpha - \beta| \gg 1$. The coherent state can equivalently be defined from the displacement operator $D(\alpha) = e^{\alpha\hat{a}^\dagger - \alpha^*\hat{a}}$ as a displaced vacuum state $|\alpha\rangle = D(\alpha)|0\rangle$ [1].

If our quantum harmonic oscillator is exposed to thermal noise it might not initially be in the vacuum state and have some population in higher Fock states. In Appendix A.1 I derive the distribution of thermal excitations in the harmonic oscillator. The thermal state of light has a Bose-Einstein distribution. In terms of temperature, T, this can be written as

$$P_n = \frac{1}{Z} e^{-\hbar\omega(n+\frac{1}{2})/k_B T}, \tag{2.9a}$$

$$Z = \frac{e^{\frac{\hbar\omega}{2k_B T}}}{e^{\frac{\hbar\omega}{k_B T}} - 1}, \tag{2.9b}$$

where k_B is Boltzmann's constant and $\hbar$ is Planck's constant. As seen in Appendix A.1, we can rewrite this in terms of the average photon number as

$$P_n = \frac{\bar{n}^n}{(\bar{n}+1)^{n+1}}. \tag{2.10}$$

The distributions of the coherent state and the thermal state can be seen in Figure 2.2.

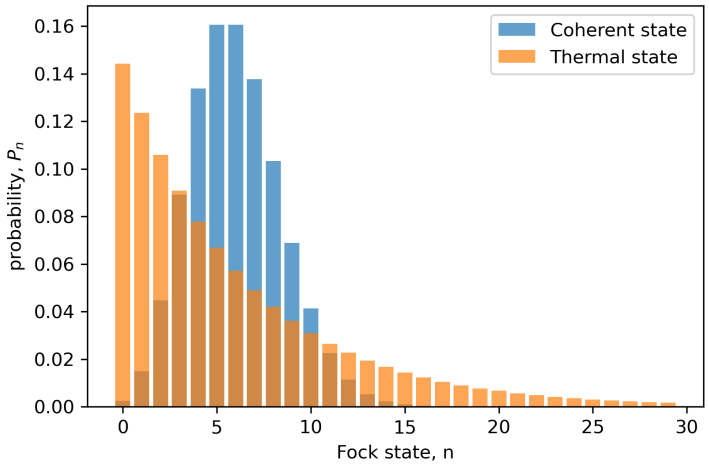

Figure 2.2: Photon number distribution of a coherent state and a thermal state simulated in QuTiP [19], [20], both with average photon number $\bar{n} = 6$. The thermal state has a Bose-Einstein distribution while the coherent state is Poissonian.

Displacing the thermal state gives a state whose distribution is beyond the scope of this project, but we can simulate it using QuTiP [19], [20]. A comparison between a displaced thermal state and coherent state (ie. a displaced vacuum state) can be seen in Figure 2.3a as well as the square root ratio between the first two populations in displaced thermal state in Figure 2.3b. For a coherent state this is simply α, which can be easily calculated from equation (2.8) as

$$\sqrt{\frac{P_1}{P_0}} = \sqrt{\frac{e^{-|\alpha|}|\alpha|^2/1!}{e^{-|\alpha|}|\alpha|^0/0!}} = |\alpha|. \tag{2.11}$$

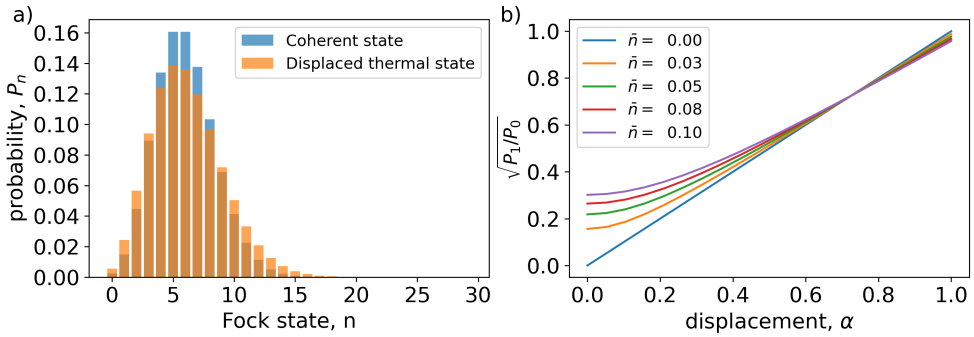

Figure 2.3: a) Photon number distribution of a displaced thermal state with average photon number $\bar{n} = 0.2$ and a coherent state (displaced vacuum, $\bar{n} = 0$). The displacement in both cases is $\alpha = 6$. b) Square root ratio of the ground state and first excited state populations for displaced thermal states with different average photon numbers.

2.2 Josephson Junctions

Two superconductors separated by a thin insulator, called a Josephson junction, has the I-V characteristic

$$I = I_0 \sin \phi, \tag{2.12a}$$

$$V = \frac{\Phi_0}{2\pi}\dot{\phi}, \tag{2.12b}$$

where I_0 is the critical current of the superconductor and $\Phi_0 = \frac{h}{2e}$ is the flux quantum [21], [22]. This characteristic gives the Josephson junction some unique properties. Firstly, at zero voltage there can be a finite DC current running through the junction. This effect is usually called the DC Josephson effect. Secondly, at finite constant voltage the phase ϕ will increase linearly meaning the current will oscillate at a frequency $\frac{\Phi_0 V}{2\pi}$. The Josephson junction and its circuit symbol can be seen in Figure 2.4.

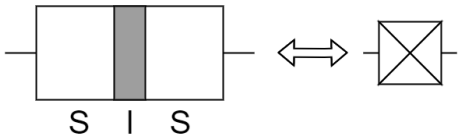

Figure 2.4: Drawing of a Josephson junction, ie. a thin insulator (I) sandwiched between two superconductors (S), and its circuit symbol.

Using the definition of inductance, $V = L\frac{dI}{dt}$, and plugging in equations (2.12a) and (2.12b) we can find that the Josephson junction has the non-linear inductance

$$L_J = \frac{L_{J0}}{\cos\phi} = \frac{L_{J0}}{\sqrt{1 - \frac{I}{I_0}^2}}, \tag{2.13}$$

where $L_{J0} = \frac{\Phi_0}{2\pi I_0}$ is called the Josephson inductance [18]. Thus, the inductance of the Josephson junction is a function of the current passing through it. Furthermore, we can calculate the total energy stored in the Josephson junction as

$$U = \int_{-\infty}^{t} I(t')V(t')dt' = E_J(1 - \cos\phi), \tag{2.14}$$

where $E_J = \frac{\Phi_0 I_0}{2\pi}$ is called the Josephson energy.

2.3 Transmon Qubits

To perform quantum computation, a linear system such as the quantum harmonic oscillator is not sufficient. We need the ability to address transitions between states separately from each other. In order to introduce some non-linearity into the system we replace the inductor of the quantum harmonic oscillator with a Josephson junction with inductance L_J and capacitance C_J (for a total capacitance $C = C_S + C_J$) as seen in Figure 2.5.

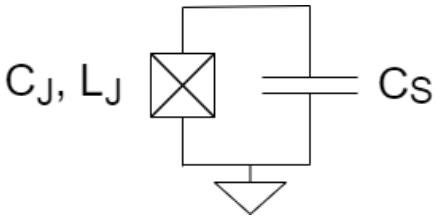

Figure 2.5: Circuit diagram for a transmon, where the inductor of the LC-resonator has been replaced by a Josephson junction.

By representing the total charge in terms of number of cooper pairs, $Q = 2em$, using equation (2.14) and promoting m and ϕ to quantized operators we can write the hamiltonian of this new system as

$$H = 4E_C\hat{m}^2 + E_J(1 - \cos\hat{\phi}), \tag{2.15}$$

with the charging energy $E_C = \frac{e^2}{2C}$ [18]. For a system with $E_J \ll E_C$ we have that $\phi \ll 1$ which lets us expand the second term and truncate it to the first non-linear correction of the harmonic oscillator Hamiltonian, which is a fourth order term. We then get a weakly anharmonic oscillator [1],

$$H = 4E_C\hat{m}^2 + \frac{E_J}{2}\hat{\phi}^2 - \frac{E_J}{4!}\hat{\phi}^4. \tag{2.16}$$

We call this type of system a transmon. As we saw in the case of the harmonic oscillator it is once again useful to introduce the creation and annihilation operators,

$$\hat{\phi} = \left(\frac{2E_C}{E_J}\right)^{1/4}(\hat{b}^\dagger + \hat{b}), \tag{2.17a}$$

$$\hat{n} = \frac{i}{2}\left(\frac{E_J}{2E_C}\right)^{1/4}(\hat{b}^\dagger - \hat{b}). \tag{2.17b}$$

We can now rewrite the Hamiltonian as

$$\begin{aligned} H &= \sqrt{8E_CE_J}\hat{b}^\dagger\hat{b} - \frac{E_C}{12}(\hat{b}^\dagger + \hat{b})^4 \\ &\approx \hbar\omega_q\hat{b}^\dagger\hat{b} - \frac{E_C}{2}\hat{b}^\dagger\hat{b}^\dagger\hat{b}\hat{b}, \end{aligned} \tag{2.18}$$

where we have used the rotating wave approximation (RWA) to neglect all terms that don't preserve the photon number [1]. As for the quantum harmonic oscillator, we can find the eigenenergies of this Hamiltonian from the eigenvalue equation, $H|n\rangle = E_n|n\rangle$, which gives us,

$$E_n = \hbar\omega n - \frac{E_C}{2}(n-1)n. \tag{2.19}$$

In this thesis we will write the first three energy levels of the transmon as $|g\rangle$, $|e\rangle$ and $|f\rangle$. The potential of the transmon can be seen in Figure 2.6.

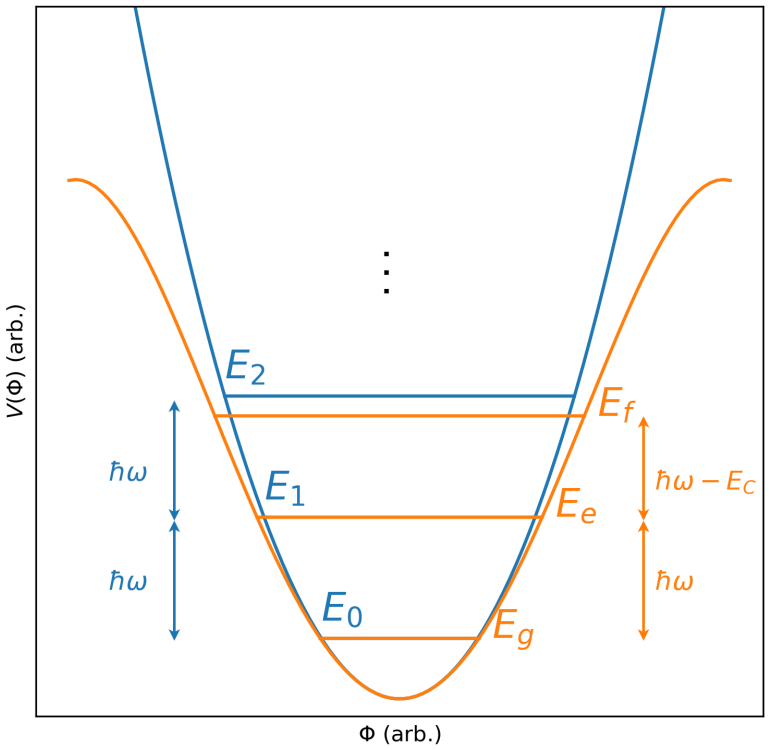

Figure 2.6: Graph of the energy potential of a harmonic oscillator (blue) and a transmon (orange) showing the first three energy levels.

With large enough E_c, meaning large anharmonicity, we can address the ground- to excited state transition separately, without transitioning to higher excited states [1], [14]. Thus, we can view the transmon as a two-level system, or a qubit. We can then model it as

$$H = -\frac{1}{2}\hbar\omega_q\hat{\sigma}_z, \tag{2.20}$$

using the Pauli z-matrix $\hat{\sigma}_z = |g\rangle\langle g| - |e\rangle\langle e|$, where $|g\rangle$ and $|e\rangle$ are the eigenstates of the two-level system corresponding to the ground state and the first excited state of the qubit, respectively [14]. Although we model our system as a two-level system it is important when working with its dynamics not to forget that the higher levels still exist.

An arbitrary state of the qubit can be written as a superposition of the ground and excited state, $|\psi\rangle = \alpha\,|g\rangle + \beta\,|e\rangle$ with $|\alpha|^2 + |\beta|^2 = 1$. It can be practical to use the equivalent representation

$$|\psi\rangle = \cos(\theta/2)\,|g\rangle + e^{i\phi}\sin(\theta/2)\,|e\rangle\,, \tag{2.21}$$

where any global phase has been omitted since it is not a physical observable. Written this way we can view the state of the qubit as a point on a sphere with coordinates $(\sin\theta\cos\phi, \sin\theta\sin\phi, \cos\theta)$, as seen in Figure 2.7. This is usually called the Bloch sphere representation of a qubit and will be used to visualize evolution of the qubit state later.

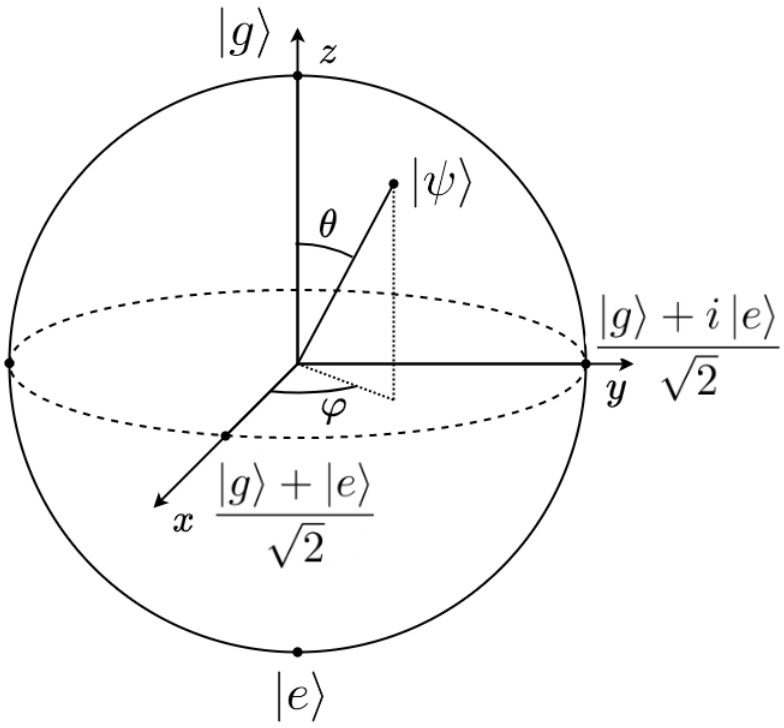

Figure 2.7: The Bloch sphere representation of the qubit. The qubit is defined by its two angles on the sphere, θ and ϕ. The ground and excited state then exist on the poles of the sphere while balanced superpositions are on the equator.

Under free evolution a qubit state evolves as $|\psi(t)\rangle = U\,|\psi(0)\rangle$, where $U = e^{i\frac{\omega_q}{2}\hat{\sigma}_z t}$ is the unitary time evolution operator. This operator rotates the state around the z-axis at frequency ω_q. We will later find it convenient to move into a rotating frame at the same frequency in which the state is stationary.

Similarly to the quantum harmonic oscillator, a transmon exposed to thermal noise will not initially be in its ground state, $|g\rangle$. In thermal equilibrium with an environment of temperature T, the probability distribution of thermal excitations in the

transmon, truncated to the three first energy levels, is

$$P_{|g\rangle} = \frac{1}{1 + e^{-\hbar\omega/k_BT} + e^{-(2\hbar\omega - E_C)/k_BT}}, \tag{2.22a}$$

$$P_{|e\rangle} = \frac{e^{-\hbar\omega/k_BT}}{1 + e^{-\hbar\omega/k_BT} + e^{-(2\hbar\omega - E_C)/k_BT}}, \tag{2.22b}$$

$$P_{|f\rangle} = \frac{e^{-(2\hbar\omega - E_C)/k_BT}}{1 + e^{-\hbar\omega/k_BT} + e^{-(2\hbar\omega - E_C)/k_BT}}, \tag{2.22c}$$

where k_B is Boltzmann's constant. These expressions are derived in Appendix A.1.

2.4 Driving the Qubit

If we continuously drive a qubit with a coherent signal at frequency ω_d we can model the system semi-classically, with the classical field being $E(t) = E\cos(\omega_d t)$ and the electric dipole moment of the qubit $\hat{d} = \vec{d}\hat{\sigma}_x$ [18]. Assuming that the electric field and the qubit dipole moment are aligned we get the interaction Hamiltonian $H_{int} = -\vec{E}\cdot\hat{d} = -A\cos(\omega_d t)\hat{\sigma}_x$, with $A = Ed$. The total Hamiltonian of the coherently driven qubit then becomes

$$H/\hbar = -\frac{\omega_q}{2}\hat{\sigma}_z - A\cos(\omega_d t)\hat{\sigma}_x \tag{2.23}$$

We can make this Hamiltonian time-independent by moving to a rotating frame, rotating at the drive frequency ω_d around the z-axis. This is done by transforming the Hamiltonian as $\tilde{H} = UHU^\dagger - iU\dot{U}^\dagger$, with the unitary transformation $U = e^{-i\frac{\omega_d}{2}\hat{\sigma}_z t}$. The Hamiltonian in the rotating frame then becomes

$$\tilde{H}/\hbar = -\frac{\Delta_d}{2}\hat{\sigma}_z - \frac{A}{2}\hat{\sigma}_x, \tag{2.24}$$

with $\Delta_d = \omega_q - \omega_d$. The eigenvalues of this Hamiltonian are

$$E_\pm = \pm\frac{\hbar}{2}\sqrt{A^2 + \Delta_d^2}, \tag{2.25}$$

and its eigenstates

$$|V_+\rangle = \cos\theta\,|e\rangle - \sin\theta\,|g\rangle\,, \tag{2.26a}$$

$$|V_-\rangle = \sin\theta\,|e\rangle + \cos\theta\,|g\rangle\,, \tag{2.26b}$$

where $\theta = \tan^{-1}\left(\frac{A}{\sqrt{A^2+\Delta_d^2}-\Delta_d}\right)$ [18]. On the Bloch sphere, these states are located on an off-kilter axis, at an angle θ from the z-axis. Under free evolution, the qubit state will precess around this axis. In Appendix A.2 I use this to derive the time-dependent excited population as

$$P_{|e\rangle} = \frac{A^2}{\Omega_R^2}\sin^2\left(\frac{\Omega_R}{2}t\right), \tag{2.27}$$

where $\Omega_R = \sqrt{A^2 + \Delta_d^2}$ is the Rabi frequency.

We can see that the excited population of a coherently driven qubit oscillates with an amplitude $A^2/\Omega_R^2 \leq 1$ with equality only when the detuning $\Delta_d = \omega_q - \omega_d = 0$. Thus, a resonant coherent drive rotates the qubit state around the Bloch sphere, around an axis on the xy-plane chosen by the phase of the drive signal. This is usually called Rabi driving. Figure 2.8 shows the qubit state under Rabi driving at different detuning as well as its population as a function of time.

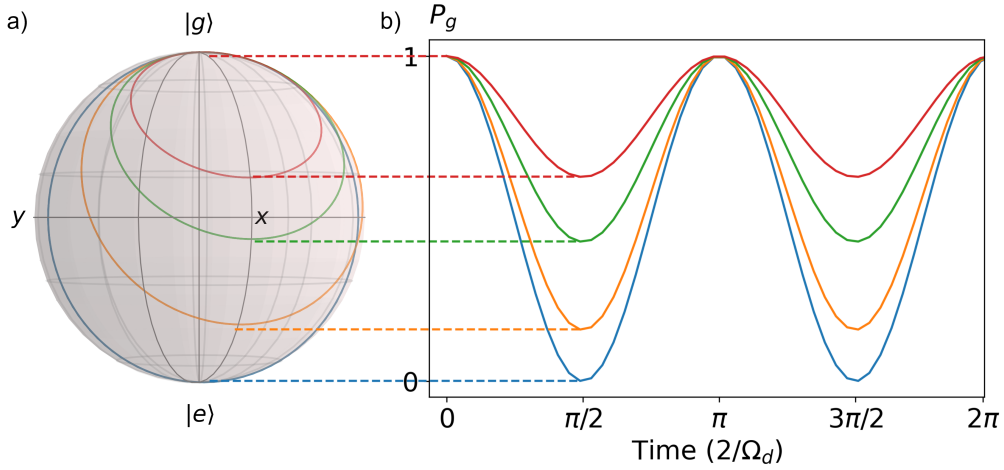

Figure 2.8: (a) Evolution of a driven qubit at different detuning, the blue curve being resonant and the others being successively more detuned. (b) The corresponding oscillations of the ground state population $P_{|g\rangle}$ at each detuning.

The amplitude of the drive determines the angular velocity of the rotation. We can choose the length and amplitude of our drive signal such that the state rotates 180° around the x-axis, for example taking it from the ground state, $|g\rangle$, to the excited state, $|e\rangle$, or vice versa. Such a signal is usually called a π-pulse. Furthermore, we may perform a pulse half as long or half as strong rotating the state 90°, for example taking the state from the ground state, $|g\rangle$, into a superposition state, $\frac{1}{\sqrt{2}}(|g\rangle + |e\rangle)$. This type of pulse is called a $\pi/2$-pulse. We will soon find these two simple rotations incredibly useful.

2.5 Coupled Harmonic Oscillator and Transmon

We can now look at what happens when we have a harmonic oscillator and a transmon capacitively coupled to each other as seen in Figure 2.9. The combined system will then be described by the Hamiltonian

$$H/\hbar = \omega_c \hat{a}^\dagger \hat{a} + \omega_q \hat{b}^\dagger \hat{b} - \frac{E_C}{2} \hat{b}^\dagger \hat{b}^\dagger \hat{b} \hat{b} + H_{int}, \tag{2.28}$$

with the interaction term

$$H_{int} = -g(\hat{b}^\dagger - \hat{b})(\hat{a}^\dagger - \hat{a}), \tag{2.29}$$

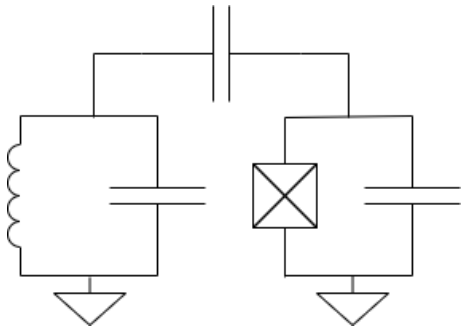

Figure 2.9: Circuit diagram of a transmon (right) and a harmonic oscillator (left) capacitively coupled to each other.

where g is the interaction strength [1]. Note that the constant term of the harmonic oscillator Hamiltonian has been omitted as compared to equation (2.4), since it doesn't affect the dynamics of the system. If $g \ll \omega_c, \omega_q$ (and $|\omega_c - \omega_q| \ll |\omega_c + \omega_q|$) we can perform the rotating wave approximation (RWA) to neglect terms that do not preserve the total photon number, $\hat{a}\hat{b}$ and $\hat{a}^\dagger\hat{b}^\dagger$. This gives us the Hamiltonian,

$$H/\hbar = \omega_c \hat{a}^\dagger \hat{a} + \omega_q \hat{b}^\dagger \hat{b} - \frac{E_C}{2}\hat{b}^\dagger\hat{b}^\dagger\hat{b}\hat{b} + g(\hat{a}^\dagger\hat{b} + \hat{a}\hat{b}^\dagger). \tag{2.30}$$

As mentioned in Section 2.3, if we are only addressing the first to energy levels of the transmon, it can be useful to model it as a two-level system. This gives us the Jaynes-Cummings Hamiltonian [18],

$$H/\hbar = \omega_c \hat{a}^\dagger \hat{a} - \frac{1}{2}\omega_q \hat{\sigma}_z - g(\hat{a}^\dagger\hat{\sigma}_- + \hat{a}\hat{\sigma}_+). \tag{2.31}$$

This Hamiltonian has the eigenvalues

$$E_g = -\hbar\frac{\Delta}{2}, \tag{2.32a}$$

$$E_\pm = (n+1)\hbar\omega_c \pm \frac{\hbar}{2}\sqrt{4g^2(n+1) + \Delta^2}, \tag{2.32b}$$

where the detuning $\Delta = \omega_q - \omega_c$. Its eigenstates, usually called dressed states, are

$$|0, -\rangle = |g\rangle\,|0\rangle\,, \tag{2.33a}$$

$$|n, -\rangle = \cos\theta_n\,|g\rangle\,|n\rangle - \sin\theta_n\,|e\rangle\,|n-1\rangle\,, \tag{2.33b}$$

$$|n, +\rangle = \sin\theta_n\,|g\rangle\,|n\rangle - \cos\theta_n\,|e\rangle\,|n-1\rangle\,, \tag{2.33c}$$

where $\theta_n = \frac{1}{2}\arctan\left(\sqrt{n+1}\frac{2g}{\Delta}\right)$, $n \geq 1$ [18]. Figure 2.10 illustrates the eigenenergies of the coupled system as compared to the separate systems.

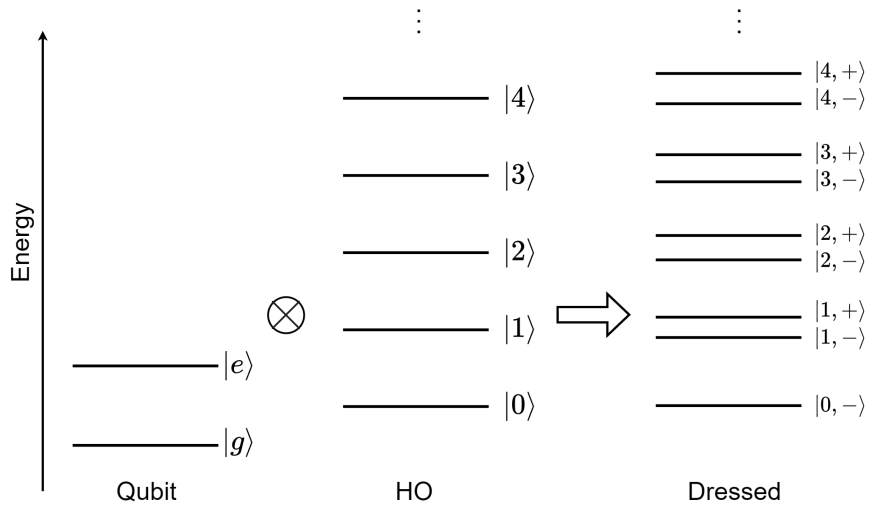

Figure 2.10: Eigenenergies of the dressed states of the coupled system compared to the energies of the two separate systems it is made of, the transmon qubit truncated to its first two energy levels and the harmonic oscillator. Here $g \ll \Delta \ll \omega_c, \omega_q$.

In the dispersive regime, where $\Delta \gg g$, the interaction Hamiltonian commutes with the bare Hamiltonian and the total Hamiltonian becomes [1]

$$H_{disp}/\hbar = \omega_c' \hat{a}^\dagger \hat{a} - \frac{1}{2}\omega_q' \hat{\sigma}_z - \chi \hat{a}^\dagger \hat{a} \hat{\sigma}_z, \tag{2.34}$$

where χ is called the dispersive shift and

$$\begin{aligned} \omega_c' &= \omega_c - \frac{g^2}{\Delta - E_C/\hbar}, \qquad \omega_q' = \omega_q + \frac{g^2}{\Delta}, \\ \chi &= \frac{g^2}{\Delta} \frac{E_C/\hbar}{(\Delta - E_C/\hbar)}. \end{aligned} \tag{2.35}$$

The frequencies ω_c' and ω_q' are the dressed frequencies and are what will be seen experimentally. Rearranging the terms of this expression, we can express the Hamiltonian as two separate systems with these new effective frequencies,

$$H_{disp}/\hbar = \omega_c' \hat{a}^\dagger \hat{a} - \frac{1}{2}\left(\omega_q' + 2\chi \hat{a}^\dagger \hat{a}\right) \hat{\sigma}_z. \tag{2.36}$$

We can interpret this as a qubit whose resonance frequency shifts by 2χ for each photon in the harmonic oscillator. Equivalently, we could write it as

$$H_{disp}/\hbar = (\omega_c' - \chi \hat{\sigma}_z) \hat{a}^\dagger \hat{a} - \frac{1}{2}\omega_q' \hat{\sigma}_z, \tag{2.37}$$

which can be interpreted as a harmonic oscillator whose resonance frequency shifts by 2χ depending on the state of the qubit. For the remainder of this thesis, the dressed frequencies will be denoted as ω_c and ω_q for simplicity.

We can exploit this property of the coupled system to determine the state of a qubit without directly measuring it, which would destroy the state in question [14]. Due to the dependence of the resonance frequency of the resonator on the state of the qubit we can probe the resonator at a fixed frequency and get a different signal back depending on which state the qubit is in. Thus, assuming that the decay rate of the resonator $\kappa \ll \chi$ so that we can resolve the shift in frequency, we are able to distinguish between the qubit ground and excited states without directly measuring it. This method of measuring the qubit state is called dispersive readout. Figure 2.11 shows the frequency characteristic of the resonator depending on the state of the qubit.

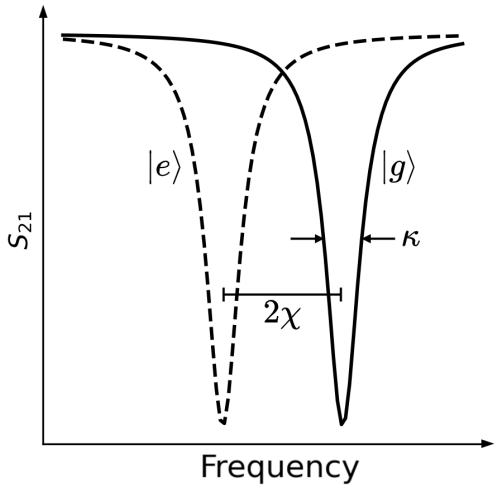

Figure 2.11: Reflection of the readout resonator when the qubit is in the ground state (solid) and excited state (dashed). The dispersive shift, χ, is defined by the separation of the two peaks and the decay rate, κ is defined by the full-width-half-maximum linewidth. If $\kappa \ll \chi$ the separate peaks can be distinguished and we can use the readout resonator for dispersive readout.

2.6 Decoherence and Noise

2.6.1 Types of Decoherence

Decoherence, ie. loss of information about a quantum state, can occur in multiple different ways when a qubit interacts with its environment, commonly referred to simply as noise. For weakly coupled noise sources, which have short correlation times, there are two characteristic types of decoherence: relaxation and dephasing. Relaxation happens when the qubit loses energy to the environment, taking it from the excited state to the ground state. An ensemble of qubit states decay exponentially at the rate

$$\Gamma_1 \equiv \frac{1}{T_1}, \tag{2.38}$$

where the relaxation time, T_1, is the time at which the average population of the ensemble becomes $1/e$ [14]. Figure 2.12 shows the average of an ensemble of qubit states at different stages of the decay process.

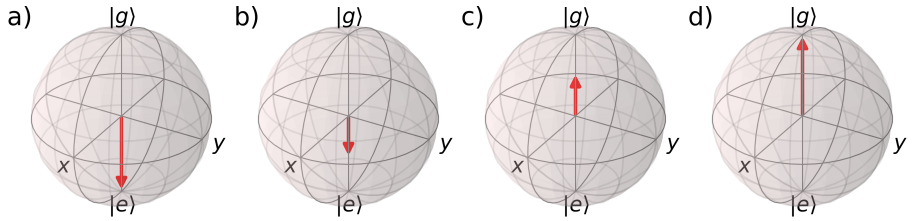

Figure 2.12: QuTiP-plot of the T1 decay. The red arrow represents the average of the states in an ensemble. a) Qubit state after being excited with a π-pulse. b-c) Average qubit state after a time $\sim T_1$. d) After a time $\gg T_1$ the entire ensemble has decayed into the ground state.

Dephasing is when information about the relative phase of a superposition state is lost. For Lorentzian noise, such as thermal noise, the rate at which an ensemble of superposition states decay can be written as

$$\Gamma_2 \equiv \frac{1}{T_2} = \frac{\Gamma_1}{2} + \Gamma_\phi, \tag{2.39}$$

where T_2 is the dephasing time [14]. The first term in this expression represents phase information being lost through relaxation and the second term represents pure dephasing. Pure dephasing comes from noise that causes fluctuations in the qubit frequency, such that the state precesses slower or faster around the z-axis. In the rotating frame, this causes the state to move forward or backward on the equator, adding some uncertainty to the states position in the xy-plane. Figure 2.13 shows an ensemble of qubit states during different stages of the dephasing process.

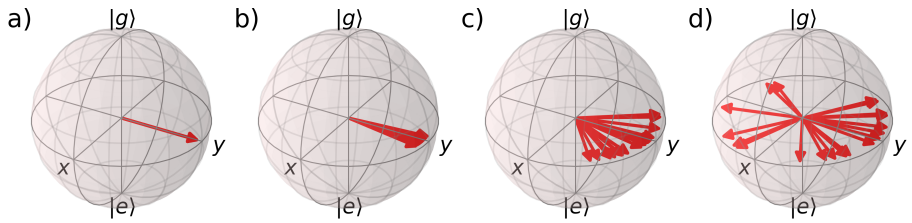

Figure 2.13: QuTiP-plot of T2 decay. Each arrow represents a single qubit state. a) Qubit state after a $\pi/2$-pulse has been applied to the qubit. b-c) After some time $\sim T_2$ the states in the ensemble have dephased. d) After a time $\gg T_2$ the states in the ensemble have lost all coherence.

2.6.2 Sources of Noise

There are many sources of noise in qubits. Some of the most common in a transmon are charge noise, flux noise and photon-induced noise [14]. Charge noise is caused by fluctuations in charge, for example due to the electric field of the capacitance

coupling to defects in the dielectric between the capacitor plates. This type of noise mainly causes energy relaxation, contributing to T_1. Additionally, low-frequency charge noise can cause fluctuation in the qubit frequency, contributing to pure dephasing. However, due to large E_J/E_C the dominant energy in a transmon is the energy stored in the Josephson junction as seen in equation (2.15), making it rather insensitive to this type of noise [14]. Flux noise arises from random fluctuations in the magnetic field that biases flux-tunable qubits, caused by flipping of spins on the superconducting surfaces of the qubit. This means flux noise is not present in non-tunable transmons, such as the ones used in this project.

Photon-induced noise is caused by fluctuations in the photon number of a resonator coupled to the qubit. Because the qubit frequency is dependent on the photon number in the cavity as seen in equation (2.36), photon number fluctuations causes fluctuations in the qubit frequency, which in turn causes pure dephasing. For times long compared to the cavity decay time, $1/\kappa$, the contribution to the pure dephasing, Γ_ϕ, from photon-induced noise is

$$\Gamma_{\text{th}} = \frac{\kappa}{2}\text{Re}\left[\sqrt{\left(1+\frac{2i\chi}{\kappa}\right)^2+\frac{8i\chi\bar{n}}{\kappa}}-1\right], \tag{2.40}$$

where κ is the cavity relaxation rate, χ is the dispersive shift and $\bar{n}$ is the average photon number in the cavity [23]. As we might expect this goes to zero at low temperature (when $\bar{n} \to 0$).

3
Experimental Setup

In this section I will explain the experimental setup used in this project including a brief overview of the functionality of the cryostat, the electronic circuitry that lets us interface with our sample as well as a look at the sample itself. Furthermore, I will explain the steps taken to characterize the sample.

3.1 Cryogenic Setup

To achieve the cryogenic temperatures necessary for a quantum device to operate, the sample was placed in a dilution refrigerator cryostat, cooling it down to approximately 10 mK. At this temperature, the rate of thermal excitations in the sample is low, allowing the qubit and resonators sufficiently long lifetimes for us to perform quantum operations on them. Additionally, the sample is housed within a microwave package that provides shielding against electromagnetic fields, further improving the lifetimes of the qubit and resonators.

The main principle of the dilution refrigerator is to utilize some special thermodynamic properties of the helium isotopes ^{3}He and ^{4}He to produce cooling [24]. At low temperatures ($\approx$ 0.87 K), a ^{3}He - ^{4}He mixture separates into two different phases. One concentrated phase consisting almost purely of ^{3}He and one dilute phase consisting mostly of ^{4}He. At this temperature the ^{4}He in the dilute phase condenses into a superfluid with zero entropy and zero viscosity while the concentrated phase remains a normal fluid. Due to the lower density of the concentrated phase it floats on top of the dilute phase [25]. Most importantly, the ^{3}He in the dilute phase has higher enthalpy than that in the concentrated phase, which means moving ^{3}He from the concentrated to the dilute phase costs energy. This energy comes in the form of heat from the environment, which leads to cooling of the system [24]. The phase diagram of a ^{3}He - ^{4}He mixture can be seen in Figure 3.1a.

In the dilution refrigerator this process takes place in the mixing chamber where the concentrated phase of ^{3}He floats atop of the dilute phase [25]. The ^{3}He is pumped through the dilute phase, causing it to consume heat. A diagram of the dilution refrigerator can be seen in Figure 3.1b. After passing through the mixing chamber, the mixture continues to the still where it is heated and nearly pure ^{3}He evaporates from the dilute phase. The ^{3}He gas is then pumped out of the cryogenic system. Outside, it is pressurized and cooled back down to about 1 K using a bath of pumped ^{4}He, before being pumped back into the system. Next, the ^{3}He gas is throttled, re-

ducing the pressure and temperature, and passes the still where heat is transferred away from it to the mixture on its way out of the system, cooling it further. It then reenters the mixture chamber, completing the cycle.

Our samples at cryogenic temperature are addressed by microwave signals sent from our instruments at room temperature through 50 Ω coaxial cables. At each temperature stage of the cryostat, the signal power needs to be comparable to the thermal energy at the temperature of that stage [24]. If the power is too small it will be buried by noise while if it is too large it will heat up the cryostat and cause additional thermal noise. Thus, the input signal needs to be progressively attenuated as it goes deeper into the cryostat. For this purpose, attenuators are placed along the input lines throughout the cryostat. The output line on the other hand needs to be amplified and thus contains a high electron mobility transistor, or HEMT, used for amplification. The wiring diagram and the cryostat itself can be seen in Figure 3.2.

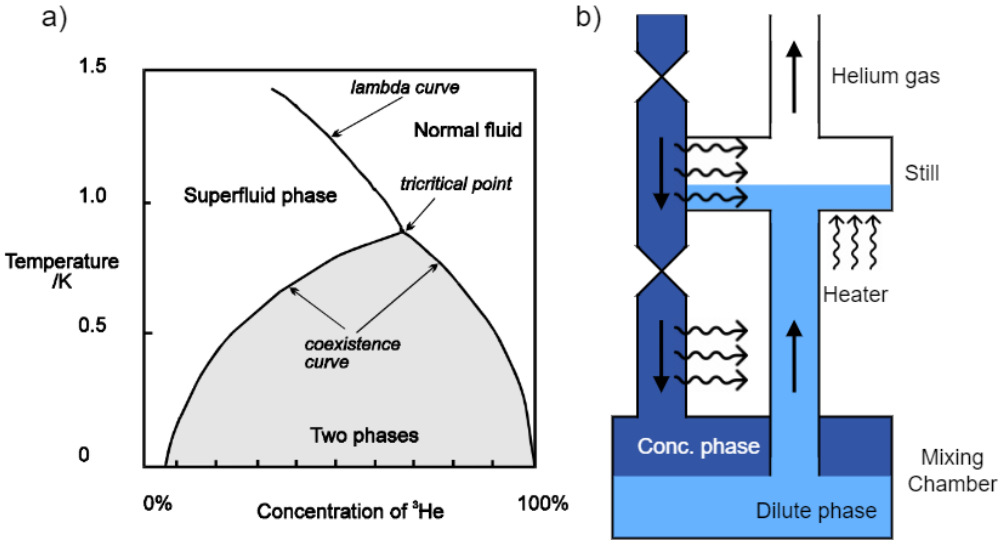

Figure 3.1: (a) Phase diagram of the ^{3}He - ^{4}He mixture, from [26]. (b) Diagram of the dilution refrigerator. Straight arrows indicate the flow of the helium and wavy arrows indicate heat flow.

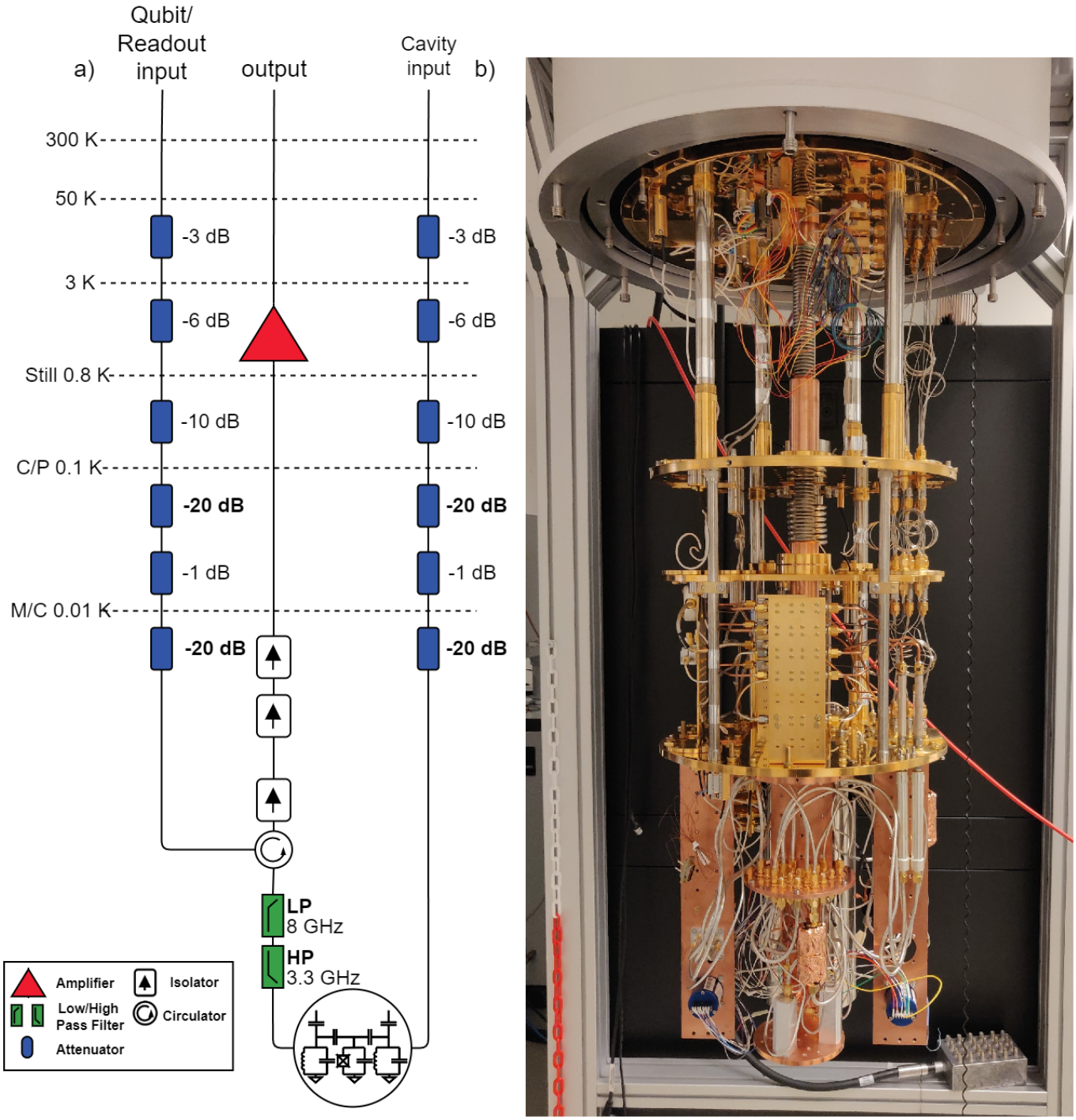

Figure 3.2: (a) Wiring diagram of the measuring setup from room temperature to the sample at approximately 10 mK. The input signals are progressively attenuated as they go further down into the dilution refrigerator. The charging lines contribute an additional -70 dB attenuation. The Output signal is amplified by a high mobility electron transition before reaching room temperature. Filters, isolators and a circulator act to further reduce noise to and from the sample. (b) Photo of the inside of the cryostat. Two 3D-cavities can be seen at the bottom. The three plates visible are the M/C plate, cold plate and still plate.

3.2 Room-Temperature Instrumentation

To generate the precise electromagnetic pulses needed to control the quantum system we used sideband mixing with in-phase-quadrature (IQ) mixers. A sine squared-shaped envelope was created by an arbitrary wave form generator (AWG) at an intermediate frequency (IF) that was then upconverted through mixing with a gigahertz frequency from a local oscillator (LO). The mixers were calibrated to minimize the unwanted higher sideband as well as LO leakage. A diagram of sideband mixing can be seen in Figure 3.3.

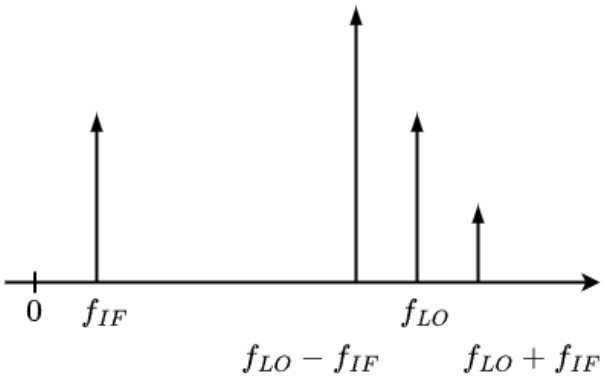

Figure 3.3: Diagram of sideband mixing. The intermediate frequency, f_{IF} is upconverted to $f_{LO} - f_{IF}$. The mixer is calibrated to minimize the upper sideband at $f_{LO} + f_{IF}$ and LO leakage.

The readout pulses were 2 µs long square pulses. In addition to the cryogenic temperature amplifiers in the dilution refrigerator, room temperature amplifiers were used to further amplify the output signals before they were downconverted to megahertz frequency.

For the arbitrary waveform generator we used a Vivace [27] which doubles as an analogue to digital converter (ADC), and for the local oscillator we used a Rohde & Schwarz sgs100a. The instruments were controlled using Labber [28] to program the pulse sequences needed for our measurements and view the results. A diagram of the room-temperature setup can be seen in Figure 3.4.

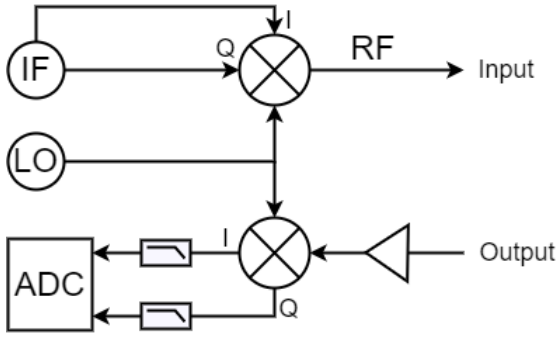

Figure 3.4: Wiring diagram of the room-temperature setup. Only the readout input and output lines are depicted. The intermediate frequency signal generated with an arbitrary waveform generator is upconverted to a radio frequency with an IQ-mixer. The signal then travels to the sample at cryogenic temperature. The output is amplified by a room-temperature amplifier and then downconverted back to the intermediate frequency. The I- and Q-components are then sent to a digitizer. The low-pass filters have a cut-off frequency of 250 MHz.

3.3 The Sample

Our sample consists of three main components: a superconducting aluminum stub-geometry three-dimensional cavity resonator, a transmon qubit and a planar microstrip resonator for dispersively reading the state of the qubit. The transmon qubit and readout resonator are fabricated from aluminum on a sapphire chip that is inserted into the cavity. The qubit is capacitively coupled to the cavity and resonator as shown in Figure 3.5a. One capacitive charging line connects to the cavity and one connects to the chip to address both the qubit and the readout resonator. A drawing of the full sample can be seen in Figure 3.5b - 3.5c.

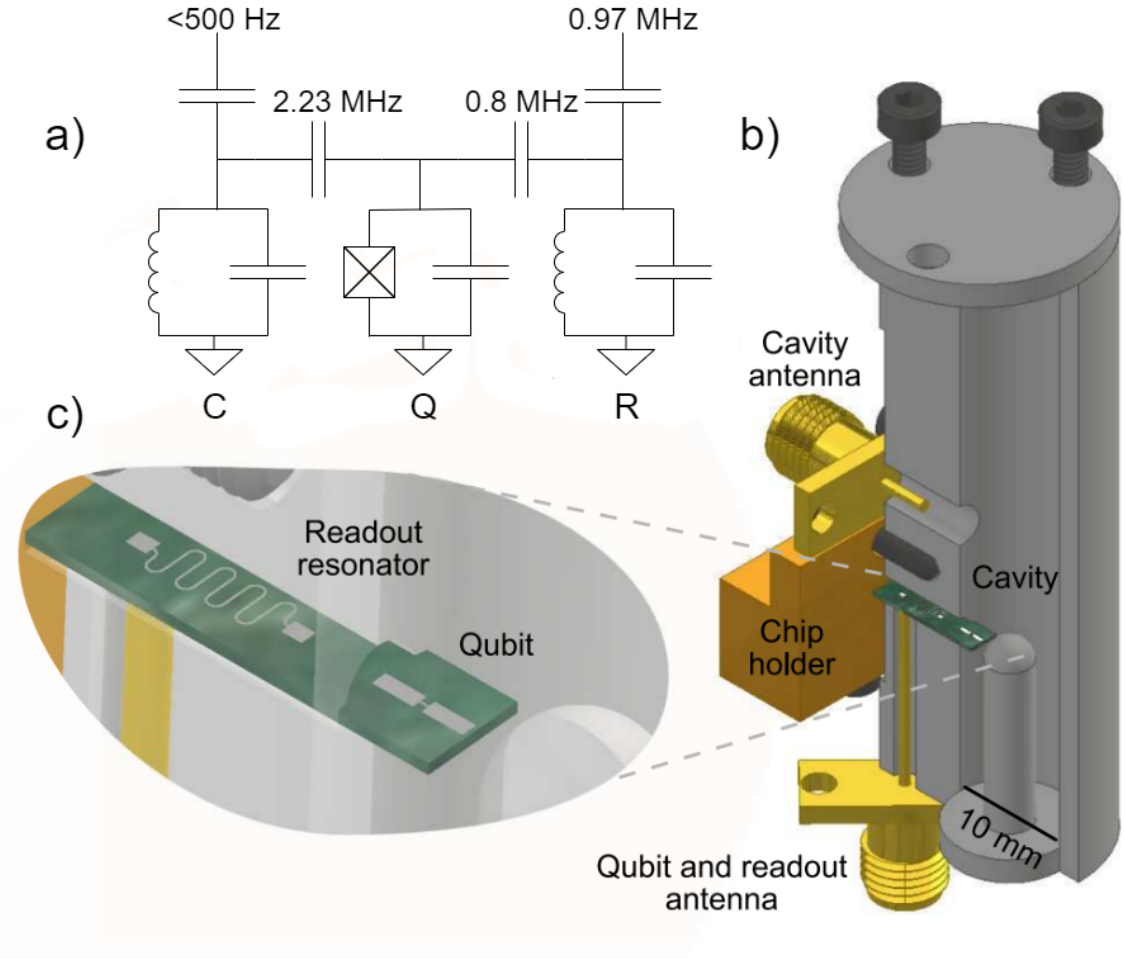

Figure 3.5: (a) Circuit diagram of the sample. C, Q and R refer to the 3D-cavity, the qubit and the readout resonator, respectively. The dispersive shift between the three components and the coupling strengths of the charging lines are written out. (b) Superconducting stub-geometry three-dimensional cavity with the sapphire chip inside. (c) Magnification of the chip containing the transmon qubit and the microstrip readout resonator. (b)-(c) adapted from M. Kudra et al. (2022) [15].

3.4 Characterization

Before we could perform any measurements on the populations in our system it had to be characterized. A number of different parameters had to be determined. To do this, a common sequence of measurements was performed, including both frequency domain and time domain measurements. The following sections describe how these measurements were performed. The results of the characterization can be seen in Table 3.1.

3.4.1 Frequency Domain Measurements

The first thing that had to be done was to find the resonance frequency, f_r, of the readout resonator, which was done by performing a one-tone spectroscopy. The

resonator was probed in reflection using a vector network analyzer (VNA), measuring the S-parameters of the resonator. The frequency dependence of the reflected signal takes a Lorentzian shape with center at the resonance frequency [24]. Thus, by fitting a Lorentzian to the data we could extract the resonance frequency, f_r as well as its decay rate, κ_r. Knowing the readout resonance frequency allowed us to perform dispersive readout as described in section 2.5.

A simple way to detect the qubit is to perform a "punch-out" measurement [18]. If the qubit and resonator are in the dispersive regime we expect the resonator frequency to be shifted as compared to its bare frequency of when it is completely uncoupled. By applying a high power signal to the resonator, the current induced in the qubit exceeds the critical current of the Josephson junction which uncouples the qubit from the resonator. Thus, by measuring the reflection of the resonator with the VNA as a function of power we could find out if the qubit and resonator are coupled and if so, at what power it becomes uncoupled. We could then pick an as high as possible power for which the two are still coupled to achieve a good signal-to-noise ratio.

With the readout frequency known we were able to find the frequency of the qubit using a two-tone spectroscopy measurement [24]. A continuous tone is then applied to the qubit. The drive frequency is then varied while dispersively reading out the qubit with the readout resonator. When the drive frequency matches the qubit resonance frequency the excited state of the qubit is populated which we can detect with the dispersive readout. This gives us a peak in the frequency characteristic, which lets us extract the qubit frequency by picking the center frequency of the peak. Once we have the qubit frequency, we can perform a similar measurement to find the frequency of the e-f transition of the qubit. To do this, we first drive the qubit at the qubit until it is in a mixed state and then repeat the two-tone spectroscopy. Since some of the population will then be in the excited state, We will see an additional peak at the e-f frequency. This measurement gives us a very rough value for the e-f frequency. The result of the two-tone measurement can be seen in Figure 3.6.

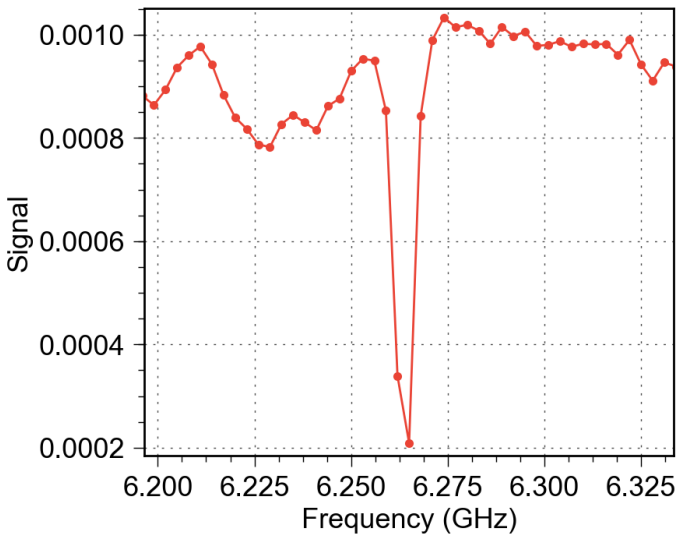

Figure 3.6: Qubit two-tone spectroscopy showing a dip at the qubit frequency, $f_q = 6.26432$ GHz.

3.4.2 Time Domain Measurements

Once we know the resonator and qubit frequencies we can start performing qubit operations. Addressing the qubit selectively at the qubit frequency, we can treat it as a two-level system. We can perform unitary operations on it by applying coherent pulses. Some of the most important pulses are the π- and $\pi/2$-pulses described in section 2.4. We can use Rabi driving to define the amplitudes for these pulses by driving the qubit and measuring it with dispersive readout as a function of amplitude. This gives an oscillation as seen in equation (2.27). We can then choose the amplitude of the π-pulse as the amplitude corresponding to half a period and the amplitude of the $\pi/2$-pulse as half of that amplitude. Repeating this measurement while also sweeping the drive frequency gives us a chevron plot.

Using pulsed measurements we can now measure the decay times T_1, T_2^* and T_2 of our qubit. A simple way of measuring T_1 is to first apply a π-pulse taking the qubit from its ground state, $|g\rangle$, to the excited state, $|e\rangle$, followed by letting the qubit decay for a time, τ, after which it is dispersively read out [14]. Averaging the result for an ensemble of states will give the ratio of qubits that decayed from which the relaxation time can be extracted. Figure 3.7 shows the pulse sequence of such a measurement.

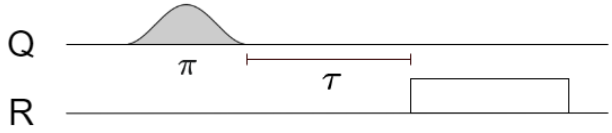

Figure 3.7: Pulse sequence used to measure the relaxation time, T_1, of a qubit. Q and R denotes the pulses targeted at the qubit and the resonator, respectively. The qubit is first moved to its excited state, $|e\rangle$, by a π-pulse. It is then let decay for some time τ after which it is read out.

To measure the dephasing time, T_2, we can first move the qubit state from the ground state, $|g\rangle$, to the equator of the Bloch sphere with a $\pi/2$-pulse, taking it to $\frac{1}{\sqrt{2}}(|g\rangle + |e\rangle)$. We then let the state decay for a time τ after which we apply a second $\pi/2$-pulse and perform a readout [14]. During the waiting time, τ, the state will gradually lose its correlation. In the rotating frame, this will appear as the states spreading out from their initial position on the Bloch sphere, eventually becoming evenly distributed around the equator having lost all phase correlation as seen in Figure 2.13. The second $\pi/2$-pulse moves the average of the ensemble back onto the z-axis. Averaging the result of the measurement then gives the decay of the ensemble. This type of measurement is called Ramsey interferometry. The pulse sequence is shown in Figure 3.8.

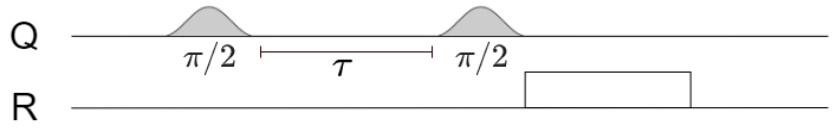

Figure 3.8: Pulse sequence used to measure the dephasing time, T_2^*, of a qubit. The qubit is first moved into a superposition state, $(|g\rangle + |e\rangle)/\sqrt{2}$, by a $\pi/2$-pulse. It is then let decay for some time τ after which it is moved back to the ground state by another $\pi/2$-pulse and read out.

The metric obtained in this way is usually denoted as T_2^*, where the asterisk indicates that the measurement was sensitive to quasi-static noise, ie. noise that is constant within a single measurement but may vary between different measurements. To make the measurement more robust against this type of noise we can perform an echo measurement [14]. We then add a π-pulse at time $\tau/2$ flipping the state over the x-axis. Within a single measurement the quasi-static noise is constant which means that any fluctuation it causes before the π-pulse will be compensated for during the waiting time after the π-pulse. For an ensemble the states spread out from their initial point on the equator during the first waiting time, then they are flipped over the x-axis and finally they refocus on the other side at time τ. The second $\pi/2$-pulse then takes the states back to the ground state. However, any fast uncorrelated noise is still present letting us extract T_2 directly. Figure 3.9 shows the pulse sequence of an echo measurement. Figure 3.10 shows how the states evolve under a T_2 echo measurement.

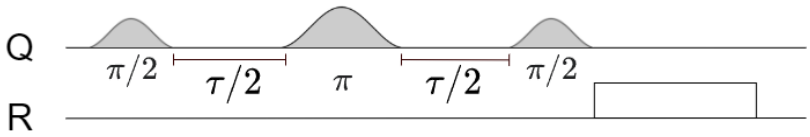

Figure 3.9: Pulse sequence used to measure the dephasing time, T_2, of a qubit. The sequence is similar to a T_2^* measurement shown in Figure 3.8 except an additional π-pulse is added in the middle of the waiting time to compensate for quasi-static noise.

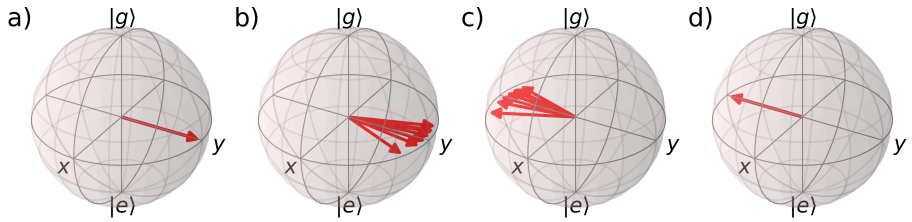

Figure 3.10: QuTiP-plot of T2 echo. a) Qubit state after a $\pi/2$-pulse has been applied to the qubit. b) Ensemble of states after some time $\tau/2$. c) Ensemble of states after applying a π-pulse. d) ensemble of states refocus after an additional time $\tau/2$.

We can also use Ramsey interferometry to get a more accurate measurement of the qubit frequency [24]. In a frame rotating at the drive frequency, the signal from the dispersive readout will oscillate at a frequency equal to the difference between the qubit frequency and the drive frequency, $\omega_q - \omega_d$. Thus, we can find a more accurate value for the qubit frequency by fitting a decaying sine curve to the oscillation and extracting the frequency detuning from that. Furthermore, we can get a more accurate measurement of the qubit e-f frequency using a pulsed measurement. To do this, we repeat the two-tone spectroscopy described above after first populating the qubit excited state with a π-pulse. We should then see a similar dip as in the regular two-tone spectroscopy, but shifted to the e-f frequency.

Figure 3.11 shows the results of the time domain characterization of the qubit.

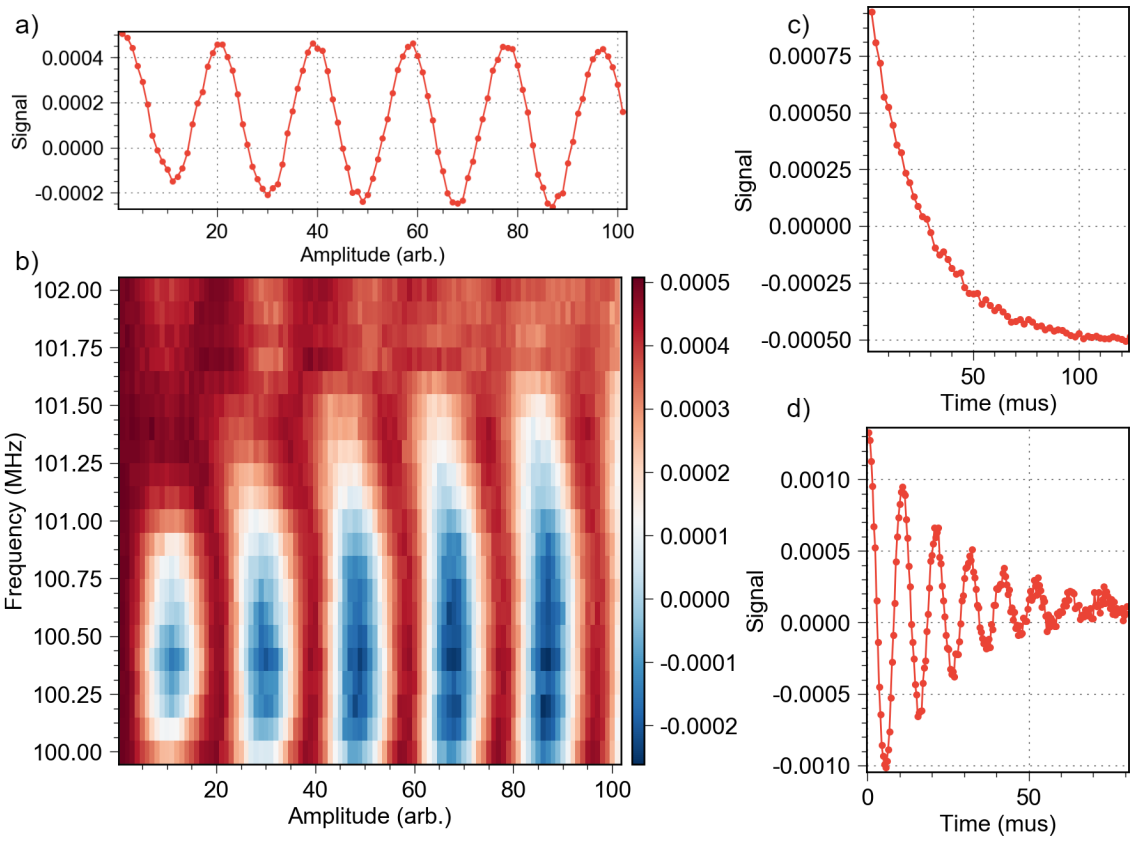

Figure 3.11: (a) Resulting signal of Rabi driving the qubit between the ground and excited state. (b) A chevron plot from Rabi driving the qubit while sweeping the frequency. The y-axis shows the intermediate frequency. The signal in a) is a cross section of the chevron plot at the maximum amplitude ($f \approx 100.4$ MHz). (c) Signal from a T_1 measurement, giving $T_1 = 24.1 \pm 1.1$. (d) Signal a T_2^* measurement using Ramsey interferometry, giving $T_2^* = 18.1 \pm 4.1$. Here the pulse sequences are off-resonant which means we see an oscillating signal. Note that the signals shown are not normalized.

Another important measurement is number splitting spectroscopy [29]. This measurement is used to find the dispersive shift between the qubit and the cavity, χ_c. It is in principle quite similar to the two-tone spectroscopy described above. As seen in equation (2.36), the qubit frequency shifts by $2\chi_c$ for each photon occupying the cavity. Thus, applying a π-pulse to the qubit at a varying frequency and then dispersively reading out the qubit, we should see a peak at the qubit frequency and then at intervals of $2\chi_c$, with heights of the peaks corresponding to the probability that the cavity is occupied by that many photons. By coherently driving the cavity before measuring, we can populate the higher Fock states enough that the multiple peaks become visible. To be able to resolve the peaks, the qubit and cavity must be in the photon number resolved regime $\kappa_c \ll \chi_c$. The number splitting spectroscopy is shown in Figure 3.12

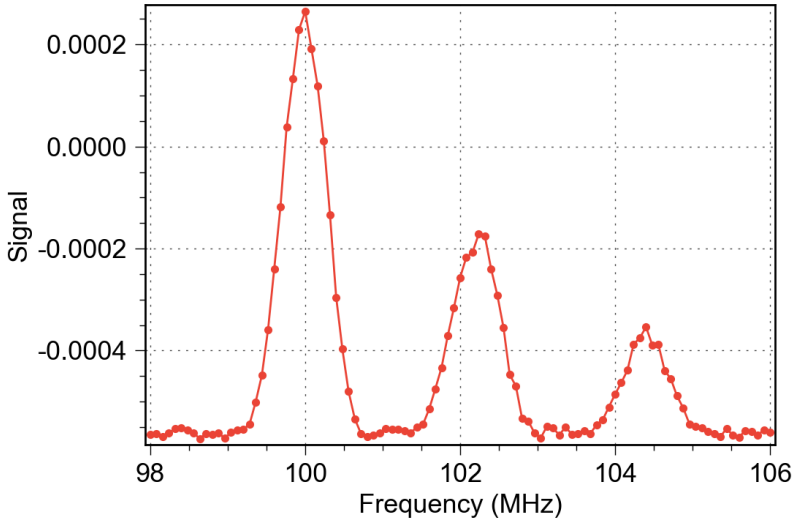

Figure 3.12: Number splitting spectroscopy of the qubit and coherently driven cavity, showing three peaks corresponding to the first three Fock states, $|0\rangle$, $|1\rangle$ and $|2\rangle$. The three peaks are distinct meaning the qubit and cavity are in the photon number resolved regime, $\kappa_c \ll \chi_c$.

Finally, we can use a pulsed measurement to fully characterize the readout resonator by applying a π-pulse before redoing the one-tone spectroscopy. Exciting the qubit causes the resonance dip of the resonator to move somewhat. By comparing the two signals we can extract the dispersive shift between the qubit and the resonator, χ_r. The result of this measurement is shown in Figure 3.13.

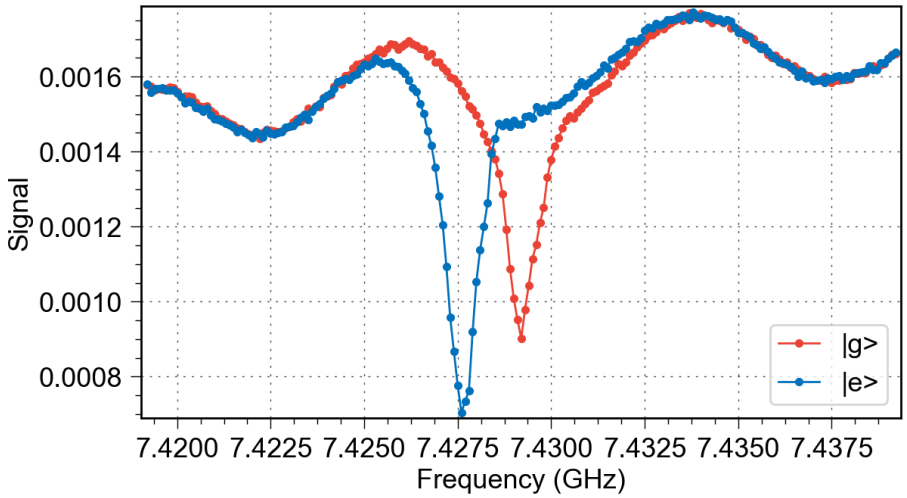

Figure 3.13: Frequency spectrum of the readout resonator with and without first applying a π-pulse taking the qubit from the ground state $|g\rangle$ to the excited state $|e\rangle$. With the excitation of the qubit the resonance frequency shifts by $2\chi_r$. The data contains a linear and a sinusoidal background which can both be removed before extracting χ_r and κ_r.

The results of the characterization can be seen in Table 3.1.

Table 3.1: Parameters characterizing the different parts of the sample. The T_1 decay time was measured 100 times, each measurement containing 101 data points of 2k averages each. The T_2^* measurement was repeated 100 times, each measurement containing 201 data points of 1k averages each. Finally, the T_2 echo measurement was repeated 51 times, each with 201 data points, with 1k averages. The errors represent one standard deviation from the average of the repeated measurements.

Cavity				
f_c [GHz]		$2\chi_c/2\pi$ [MHz]	$\kappa_c/2\pi$ [Hz]	
4.451		2.23	< 500	
Qubit				
f_{ge} [GHz]	f_{ef} [GHz]	T_1 [µs]	T_2^* [µs]	T_2 [µs]
6.26432	5.91132	24.1 ± 1.1	18.1 ± 4.1	35.2 ± 1.0
Readout				
f_r [GHz]		$2\chi_r/2\pi$ [MHz]	$\kappa_r/2\pi$ [MHz]	
7.3292		0.8	0.97	

4

Measuring Thermal Populations

In this section I present the techniques for measuring the thermal population, ie. the population caused by thermal excitations, and effective temperature in the qubit, the 3D-cavity and the readout resonator. I also present the results of those measurements. For the qubit we measure its residual excited-state population, which at low temperatures is equal to the average photon number, $P_{|e\rangle} = \bar{n}$, since the higher energy state populations are negligible. For the cavity we measure the ratio between $P_{|1\rangle}$ and $P_{|0\rangle}$ and extract the average photon number from the displaced thermal state distribution. Lastly, for the readout resonator we estimate the average photon number from the dephasing of the coupled qubit.

4.1 Qubit Thermal Population

To measure the residual excited-state population of the qubit, $P_{|e\rangle}$, we utilize Rabi driving between its first excited state, $|e\rangle$, and its second excited state, $|f\rangle$, by applying a coherent signal at frequency $\omega_{ef} \approx \omega_q - E_c/\hbar$, as described in reference [3]. Dispersively reading out the qubit driven at this frequency should provide us with an oscillating signal with amplitude $A_1 \propto P_{|e\rangle} - P_{|f\rangle}$. By first applying a π-pulse at frequency $\omega_{ge} = \omega_q$ we can swap $P_{|g\rangle}$ and $P_{|e\rangle}$ which then lets us read out an oscillation with amplitude $A_0 \propto P_{|g\rangle} - P_{|f\rangle}$ which we can use as a reference. Since the setup remains the same between measurements the proportionality constant will be the same in both cases. Assuming the qubit is cold, which is the case we are interested in, $P_{|f\rangle}$ will be small compared to $P_{|e\rangle}$ which will be small compared to $P_{|g\rangle}$. Thus we can neglect $P_{|f\rangle}$. This lets us calculate the residual population as [3]

$$P_{|e\rangle} = \frac{A_1}{A_0 + A_1}. \tag{4.1}$$

Because we are using dispersive readout on the ground state of the qubit, we have to apply an additional π-pulse after the e-f Rabi driving to move the oscillating population back into the ground state. The pulse sequence and the corresponding populations in each state can be seen in Figure 4.1. For this measurement the pulse length of the qubit pulses were chosen to 2 µs. Once the data had been obtained, a sine curve of the form $A\cos(\omega t + \phi) + K$, where A, ω, ϕ and K are fitting parameters, was fitted to both the signal and the reference to extract their amplitudes. The result of a typical measurement can be seen in Figure 4.3a. Averaging the results of 20 repetitions of the measurement gave a residual excited population of $P_{|e\rangle} = 0.0025 \pm 0.0006$, where the error represents one standard deviation of the measurements.

Each repetition measured 200 data points that were each an average of 20k shots. We can use the distribution in equations (2.22) to find an effective temperature of the qubit, ie. the temperature at which the qubit would have the population we measure if it was in thermal equilibrium. This gives an effective temperature of $T_{eff} \approx 50.2 \pm 1.9$ mK.

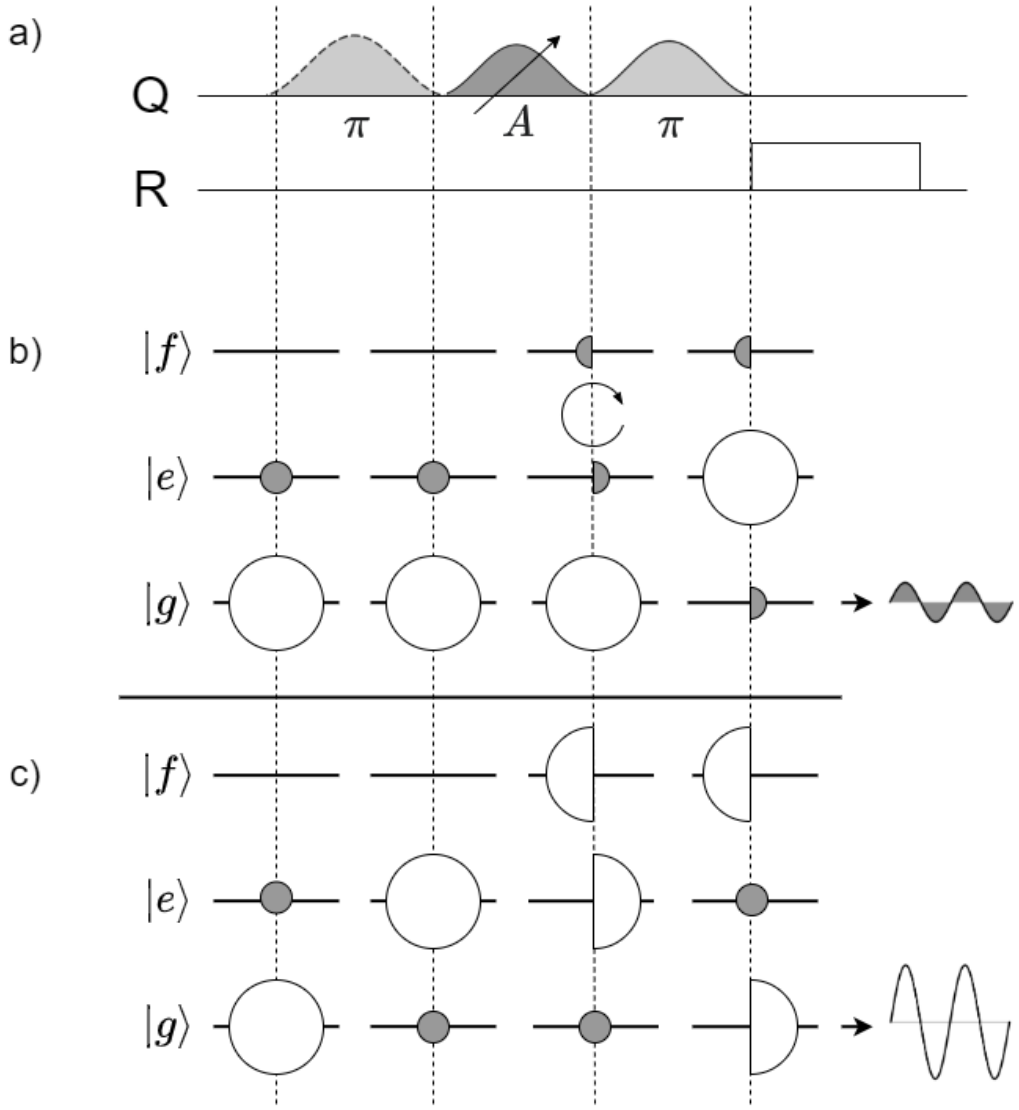

Figure 4.1: (a) Pulse sequence for measuring the residual excited-state population. The light gray pulses are at the qubit frequency, $\omega_{ge} = \omega_q$. The dark gray pulse represents e-f Rabi driving at frequency $\omega_{ef} = \omega_q - E_c/\hbar$. The dashed outline of the first π-pulse indicates that it is included or excluded depending on whether we want to measure the signal or the reference. (b)-(c) Corresponding population in each qubit state at different stages of the measurement. The white and gray disks represent the populations initially in the ground- and excited state, respectively. The half disks represent the oscillating populations when the qubit is driven. Depending on how much it was driven, different proportions of the initial population will be in each half disk. (b) and (c) shows the populations when the dashed π-pulse is excluded and included, respectively. In the first case we read out a signal proportional to the initial excited state population, $P_{|e\rangle}$, while in the latter case we read a signal proportional to the initial ground state population, $P_{|g\rangle}$, which we use as reference.

As a way of validating the method, it is useful to perform the measurement at multiple different effective temperatures. To do this we need to manually populate the qubit before we measure it. A simple way of populating the qubit is to excite it to its excited state with a π-pulse and then let it decay for some time τ. Because

we know the decay rate of the qubit (see Table 3.1), we can determine what the population should be after a duration τ.

For this purpose we repeat the measurement with an added π-pulse and waiting time. This extended pulse sequence can be seen in Figure 4.2. The typical result of measuring the populated qubit can be seen in Figure 4.3b. A clear increase in amplitude of the signal and a corresponding decrease in the amplitude of the reference as compared to the non-populated case can be seen. The results of measurements as a function of the waiting time, τ, is shown in Figure 4.3d. Fitting an exponential decay to this the same way we would for a regular T_1 measurement gives us a decay time of $T_1' = 15.9 \pm 0.5$ µs, where an apostrophe is used to indicate that this value was not obtained with the standard T_1 measurement. Notably, this decay rate is significantly smaller than the actual T_1 of the qubit seen in Table 3.1. A possible explanation of this discrepancy is that the qubit wasn't undisturbed and allowed to decay freely before the readout. Instead, some pulses were applied to it and it was partially excited to the second excited state. This interaction may account for the difference in the measurements.

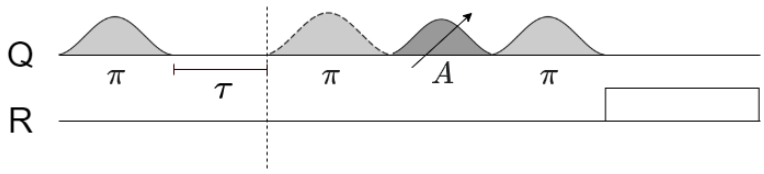

Figure 4.2: Extended pulse sequence from Figure 4.1 to measure the qubit at different populations. Left of the dashed line are the added elements used to populate the qubit before a measurement.

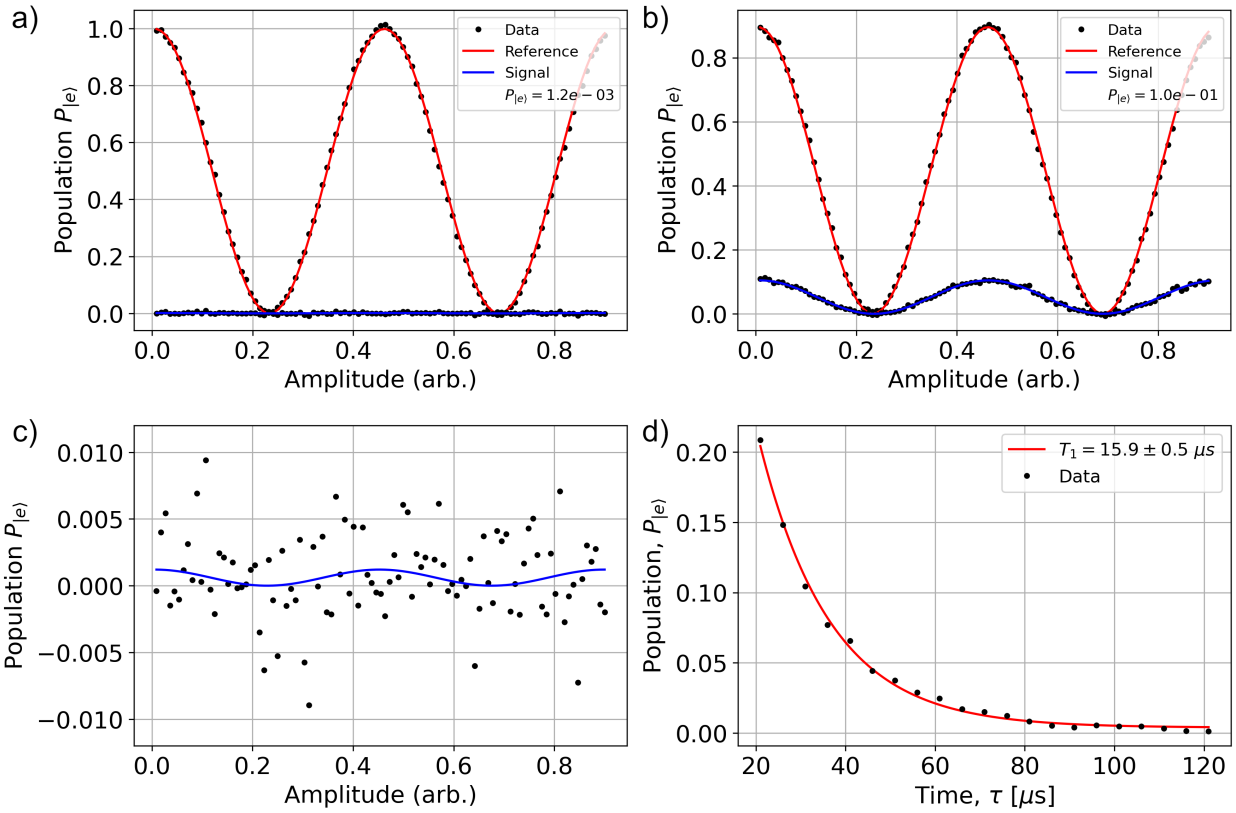

Figure 4.3: a) Typical result of a qubit thermal population measurement. b) Typical result of a qubit thermal population measurement, after the qubit has been populated with a π-pulse and let decay for $\tau \approx 26$ µs. In both plots a sine curve has been fitted to the signal data (blue) and the reference data (red). c) Zoom-in on the signal data and fit from a). We can see that the signal-to-noise ratio is very small for small populations. No significant signal can be distinguished from the noise in this plot. d) Measured populations at different times after populating the cavity with a π-pulse. An exponential decay has been fitted giving a relaxation time of $T_1' = 15.9 \pm 0.5$ µs.

4.2 Cavity Thermal Population

For measuring the thermal population in the cavity two different methods were used, one based on Rabi driving and one based on Ramsey interferometry. The two methods were then compared to each other.

4.2.1 Measuring the Population with Rabi Driving

The first method used to measure the thermal population in the cavity is based on Rabi driving. This type of measurement was previously done in reference [16]. According to equation (2.36) the qubit frequency depends on the number of photons in the cavity as $\omega_n = \omega_q + 2n\chi$. Thus, for an ensemble of states, driving the qubit at frequency ω_n and dispersively reading out, we should get a oscillating signal with an amplitude proportional to the population in the cavity state $|n\rangle$, $A_n \propto P_n$. From equation (2.10) we can see that for small thermal states the average photon number

in the cavity is approximately equal to the ratio of the population in the first excited state and the ground state, $P_1/P_0 \approx \bar{n}$. With this in mind we perform two separate measurements. First we drive the qubit at frequency $\omega_0 = \omega_q$ followed by dispersive readout. We then repeat the same measurement at frequency $\omega_1 = \omega_q + 2\chi$. The proportionality constant between the cavity populations and the readout voltage remains the same across measurements. It follows that the average photon number can be calculated as the ratio between the signal amplitude, A_1, and the reference amplitude, A_0. An analytical derivation of this result can be found in Appendix A.3. The pulse sequence for the measurement can be seen in Figure 4.4. Similarly to the qubit thermal population measurement we now want to be highly selective and therefore again use pulses of length 2 µs. Because the two frequencies used in this measurement are so close to each other, it is important to not increase the amplitude too much while still using relatively short pulses lest the spectral width becomes too broad. Thus, only four periods were measured for each run. A sine curve with a linear background of the form $A\cos(\omega t + \phi) + Bt + K$ was fitted to the signal and reference. Additionally, the frequency ω was constrained to be the same for both sines. The typical result of a measurement can be seen in Figure 4.5a.

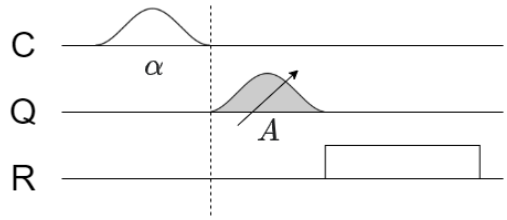

Figure 4.4: Pulse sequence for measuring the cavity thermal population using Rabi driving. C, Q and R denotes the pulses targeted at the cavity, the qubit and the resonator, respectively. The measurement is performed twice. Once driving the qubit at $\omega_0 = \omega_q$ and once at $\omega_1 = \omega_q + 2\chi$. Left of the dashed line is the part of the sequence used to populate the cavity before a measurement which consists of a coherent displacement.

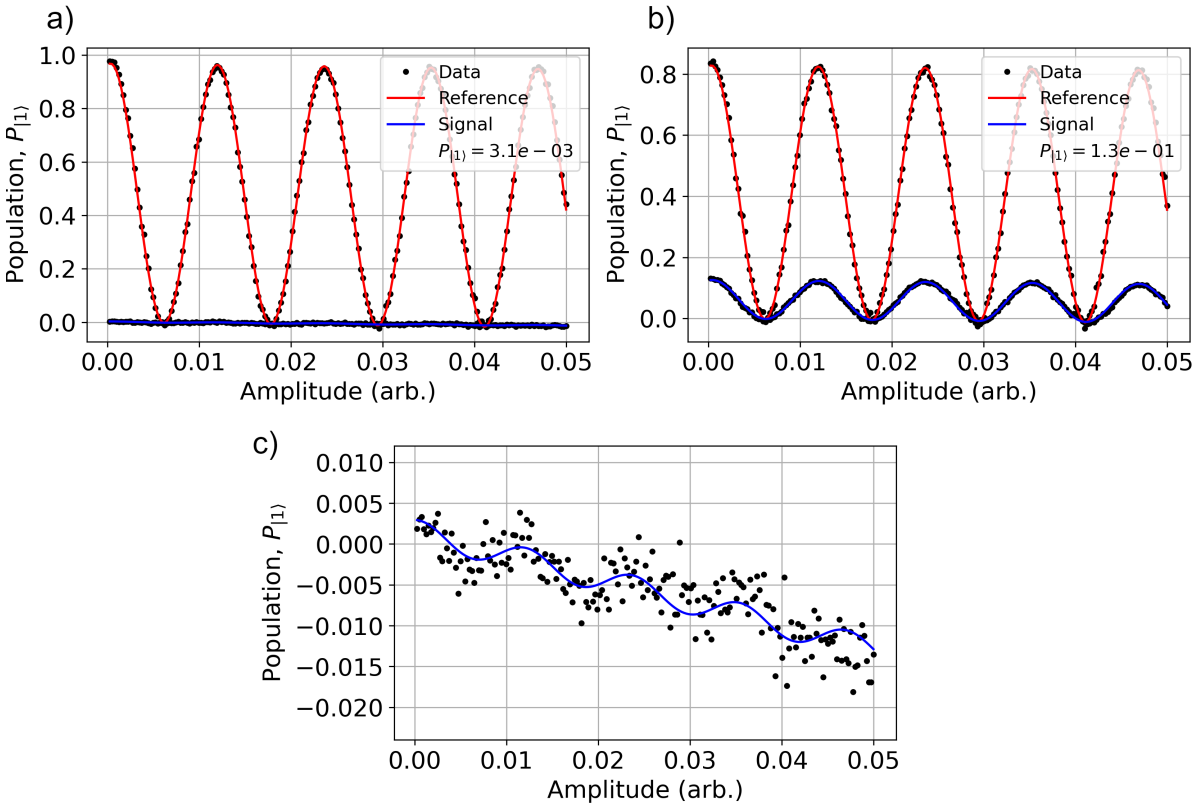

Figure 4.5: (a) Typical result of cavity thermal population measurement using Rabi driving. The measurement contains 201 datapoints for the signal and 201 for the reference. The reference data points are averages of 2k shots while the signal data points are averages of 20k shots. (b) Typical result of cavity thermal population measurement using Rabi driving after the cavity has been populated using a coherent pulse, as described in Section 4.2.3. In both plots a sine curve has been fitted to the reference data (red) and the signal data (blue). c) Zoom-in of the signal data and fit from a). In this plot we can very clearly see a sloped background. It is unclear what causes this.

4.2.2 Measuring the Population with Ramsey Interferometry

The second method for measuring the cavity population is based on Ramsey Interferometry. Similarly to the previous method we utilize the fact that the qubit frequency is dependent on the cavity photon number, n as seen in equation (2.36). To measure the populations we first apply an off-resonant $\pi/2$-pulse, taking the qubit to a superposition state. In a rotating frame at drive frequency ω_d, the qubit state will precess around the z-axis at frequency $(\omega_q - 2n\chi) - \omega_d$. After letting the state evolve freely for some time τ another identical $\pi/2$-pulse is applied. Reading out the state with dispersive readout should then give a sum of oscillating signals at frequencies $(\omega_q - 2n\chi) - \omega_d$ and amplitudes $A_n \propto P_{|n\rangle}$. Similarly to the first method, for small thermal states, we can calculate the average photon number as the ratio between the signal amplitude, A_1, and the reference amplitude, A_0. This result is derived in Appendix A.4. The pulse sequence of this measurement can be seen in Figure 4.6. Unlike for the previous two measurements, we want to be very un-selective to be able

to drive multiple frequencies ω_n simultaneously. Thus, a pulse length of 50 ns was used for the qubit pulses. Additionally, for the highest possible frequency resolution we want the measurement to be long in time domain. However, we don't want it to be long enough that the qubit relaxation and decay plays a significant role. Taking those two factors into account we choose a time step between data points such that $Ndt \approx 2T_2$, where $N = 301$ is the number of datapoints and $dt = 100$ ns is the time step. We then choose the detuning of the off-resonant pulses such that both the signal frequency and the reference frequency lie below the Nyqvist frequency $f_N = 1/(2dt)$ while not being significantly smaller than it. The detuning was chosen to $\Delta f = 2$ MHz. Since the dispersive shift in our system is negative, meaning the qubit frequency decreases with each photon in the cavity, we choose to put the drive frequency at a higher value than the qubit frequency. That way we avoid overlap between the two. Once the data has been measured we fit a sum of two decaying sine curves to it, of the form $[A_0 \sin(\omega_0 t + \phi_0) + A_1 \sin(\omega_1 t + \phi_1)]\, e^{-t/T_2}$. Since the populations of higher Fock states are negligible in a cold cavity it is reasonable to only fit sine curve corresponding the two first Fock states. A typical result of the measurement can be seen in Figure 4.7a. Figure 4.7c shows the Fourier transform of the data.

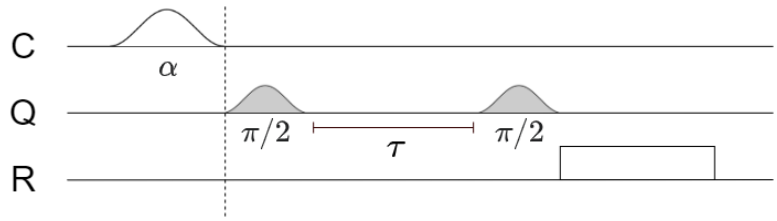

Figure 4.6: Pulse sequence for measuring the cavity thermal population using Ramsey interferometry. The qubit is taken to a superposition state by an off-resonant $\pi/2$-pulse after it is let evolve for some time τ and then taken back by an identical $\pi/2$-pulse. Left of the dashed line is the part of the sequence used to populate the cavity before a measurement which consists of a coherent displacement.

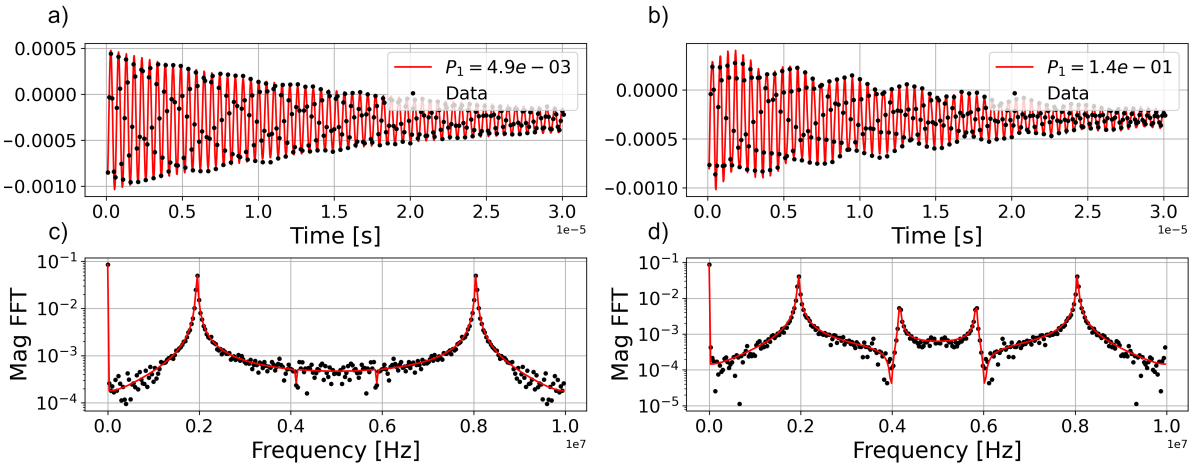

Figure 4.7: (a) Typical result of a cavity population measurement using Ramsey interferometry. The measurement contains 301 data points with 20k averages. (b) Typical result of a cavity population measurement using Ramsey interferometry after populating the cavity with a coherent displacement, as described in Section 4.2.3. In both plots a sum of two decaying sine curves has been fitted to the data. (c)-(d) Magnitude of the Fourier transform of the data as well as the fitted function in (a) and (b). Here we can clearly see an additional peak appear after populating the cavity.

4.2.3 Comparing the Methods

To confirm that these two methods produce results that are consistent with our theoretical model we need to perform the measurements at a wide range of different populations. To do this, the measurements were both performed after first applying a coherent displacement, $D(\alpha)$, to the cavity with varying amplitude, α. This creates a displaced thermal state in the cavity for which the populations could be calculated using QuTip [19], [20] as demonstrated in Figure 2.3. The resulting function was then fitted to the measured data to find a value for $\bar{n}$. The results of a typical measurement of a populated cavity using Rabi driving and Ramsey interferometry can be seen in Figure 4.5b and 4.7b, respectively. In both cases we see a very clear increase in the amplitude of the signal oscillation accompanied by a similar decrease in the amplitude of the reference when the cavity is populated before the measurement, as expected.

Figure 4.8 shows the data measured using Rabi driving and Ramsey interferometry at different displacements, both with 6k averages per data point. Fitting the square root ratio of the first excited population and the ground state population for a displaced thermal state, the average photon number was estimated to be $\bar{n} = 0.0037 \pm 0.0011$ using Rabi driving and $\bar{n} = 0.0059 \pm 0.0013$ Ramsey interferometry, where the errors are the standard deviation from the fitted curve. While both methods agree well with the fitted theoretical prediction, the data obtained using Rabi driving appears to be somewhat more accurate, hence the smaller error. Using the measured values for the average photon number and the distribution in equation (2.9) we can calculate an effective temperature. We then get an effective

temperature of $T_{eff} = 38.2 \pm 1.2$ mK using Rabi driving and $T_{eff} = 41.7 \pm 1.9$ mK using Ramsey interferometry.

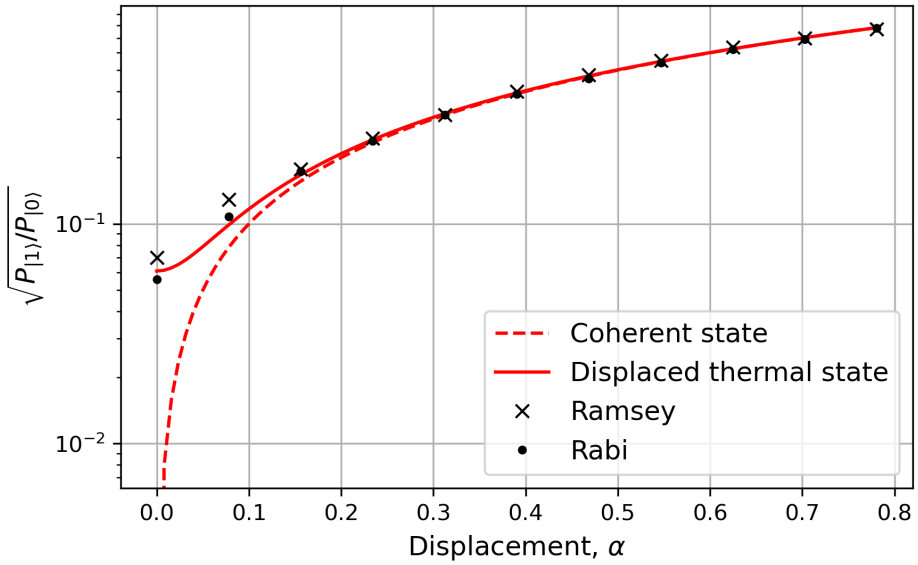

Figure 4.8: Square rooted ratio of excited state population and ground state population of the cavity after displacing it with a coherent drive, measured using Rabi driving and Ramsey interferometry with 6k averages per data point. The solid red line shows the theoretical prediction using the distribution of a displaced thermal state, fitted to the data points obtained using Rabi driving with the average photon number, $\bar{n}$, as fitting parameter. This gives an average photon number of $\bar{n} = 0.0037 \pm 0.0011$. Doing the same fit using the data points obtained with Ramsey interferometry gives $\bar{n} = 0.0059 \pm 0.0013$. The dashed line shows the prediction for a displaced thermal state with $\bar{n} = 0$, ie. a coherent state, which is notably just α.

Figure 4.9 shows the data measured with 20k averages per data point, taken at smaller displacements. The method based on Rabi driving works well even at lower displacements (with increased number of averages), agreeing well with a displaced thermal state with average photon number $\bar{n} = 0.0034 \pm 0.0003$, where the error is the standard deviation. However, the method based on Ramsey interferometry performs significantly worse below a certain threshold at approximately $\alpha = 0.1$. Below this threshold the variance between the data points increases drastically, as seen in Figure 4.9. This might be because a limiting factor when measuring using Ramsey interferometry is the relative size of the signal and the reference. When the signal becomes too small compared to the reference, $A_1 \ll A_0$, the fitting tool is unable to distinguish the signal from the reference. Since the method using Rabi driving measures the signal and reference separately it doesn't have the same problem and the only limiting factor is the signal-to-noise ratio. Presumably the threshold at which the population can no longer be measured using Ramsey interferometry could be lowered by further increasing the number of averages. Calculating the effective temperature for the measured population gives a value of $T_{eff} = 37.6 \pm 0.3$ mK.

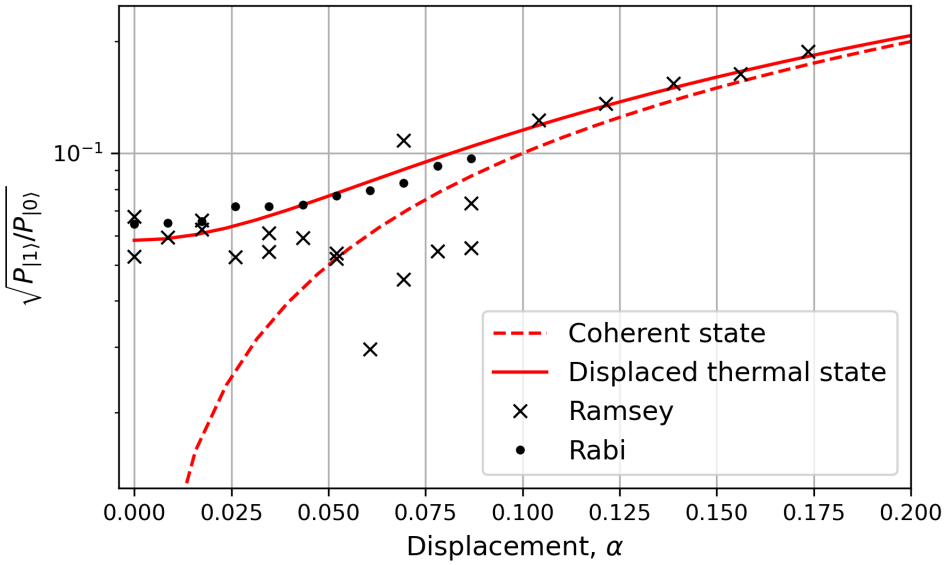

Figure 4.9: Square rooted ratio of excited state population and ground state population of the cavity after displacing it with a coherent drive, measured using Rabi driving and Ramsey interferometry with 20k averages per data point. Fitting the theoretical prediction of a displaced thermal state to the data points obtained with Rabi driving gives an average photon number $\bar{n} = 0.0034 \pm 0.0003$. While the data obtained using Rabi driving agrees well with the prediction, the method using Ramsey interferometry seems to fail below a certain threshold at approximately $\alpha = 0.1$.

4.3 Readout Resonator Thermal Population

Directly measuring the thermal population in the readout resonator would not be possible because the qubit and resonator are not deep in the photon number resolved regime ($\kappa_r \ll \chi_r$). However, we can estimate an upper bound using the photon-induced dephasing in equation (2.40). Assuming that the pure dephasing of the qubit is solely due to photon number fluctuations in the readout resonator, $\Gamma_\phi = \Gamma_{\text{th}}$, we can plug equation (2.40) into equation (2.39) and extract the thermal population, $\bar{n}$. Using the values from Table 3.1, we then get the upper bound $\bar{n} < 0.0018$ corresponding to a temperature $T_{eff} < 56.1$ mK. Due to the readout resonator's proximity to the cold environment we expect it to be the coldest among the three components. However, since the estimated upper limit for the temperature is larger than measured temperatures of the qubit and the cavity, we cannot confirm whether this is the case.

5

Quality Factor Measurement

In addition to the main goal of this thesis, one objective was to characterize the quality factor of a niobium 3D-cavity. Niobium is a commonly used alternative to aluminum which can potentially provide a higher quality factor [17]. In this section I explain the method used to measure the internal quality factors of the Nb cavity. I then present the results obtained this way.

To obtain the quality factors, the S-parameters of the cavity are first measured using a VNA. The quality factors are then extracted using a circle fit. The transmission signal of the cavity can be written as [6]

$$S_{21}(f) = ae^{i\alpha}e^{-2\pi i f\tau}\left[1 - \frac{(Q_l/|Q_c|)e^{i\phi}}{1 + 2iQ_l(f/f_r - 1)}\right], \tag{5.1}$$

where Q_i is the internal quality factor, Q_c is the coupled quality factor and $1/Q_l = 1/Q_i + 1/Q_c$ is the loaded quality factor. The expression inside the brackets is that of an ideal resonator. ϕ accounts for asymmetries in the transmission signal caused by impedance mismatch and other imperfections in the measurement setup. In the complex plane, $(\mathrm{Re}[S_{21}], \mathrm{Im}[S_{21}])$, this expression traces out a circle of radius $Q_l/|Q_c|$. The circle intersects the x-axis at two points. Once at unity for $f = \pm\infty$ and once at $1 - Q_l/|Q_c|$ for $f = f_r$. However, with a non-zero ϕ the circle is tilted somewhat such that the resonance frequency is above or below the x-axis. The rate at which phase is acquired along the circle as frequency increases is Q_l. Thus we can extract the internal and external quality factors from an ideal resonator by fitting a circle and parametrizing it with the phase. However, there are some imperfections from outside the resonator itself such as loss and electric phase-delay that are accounted for in the two factors outside the brackets. Here, a and α are the attenuation and phase shift in the cables and τ is the electronic delay caused by the length of the cables. While it is possible to minimize these effects by careful calibration of the VNA that's not always easy. Instead we can compensate for them when fitting the data. A more detailed explanation on how this is done can be found in reference [6]. A typical result of the circle fit can be seen in Figure 5.1. Figure 5.2 shows the resulting Q_i measured at different powers. At powers above ≈ -120 dBm we see a quality factor of approximately 4.3 million, which is an expected result for an unpolished cavity. The next step would be to polish the cavity and remeasure it, which is beyond the scope of this thesis.

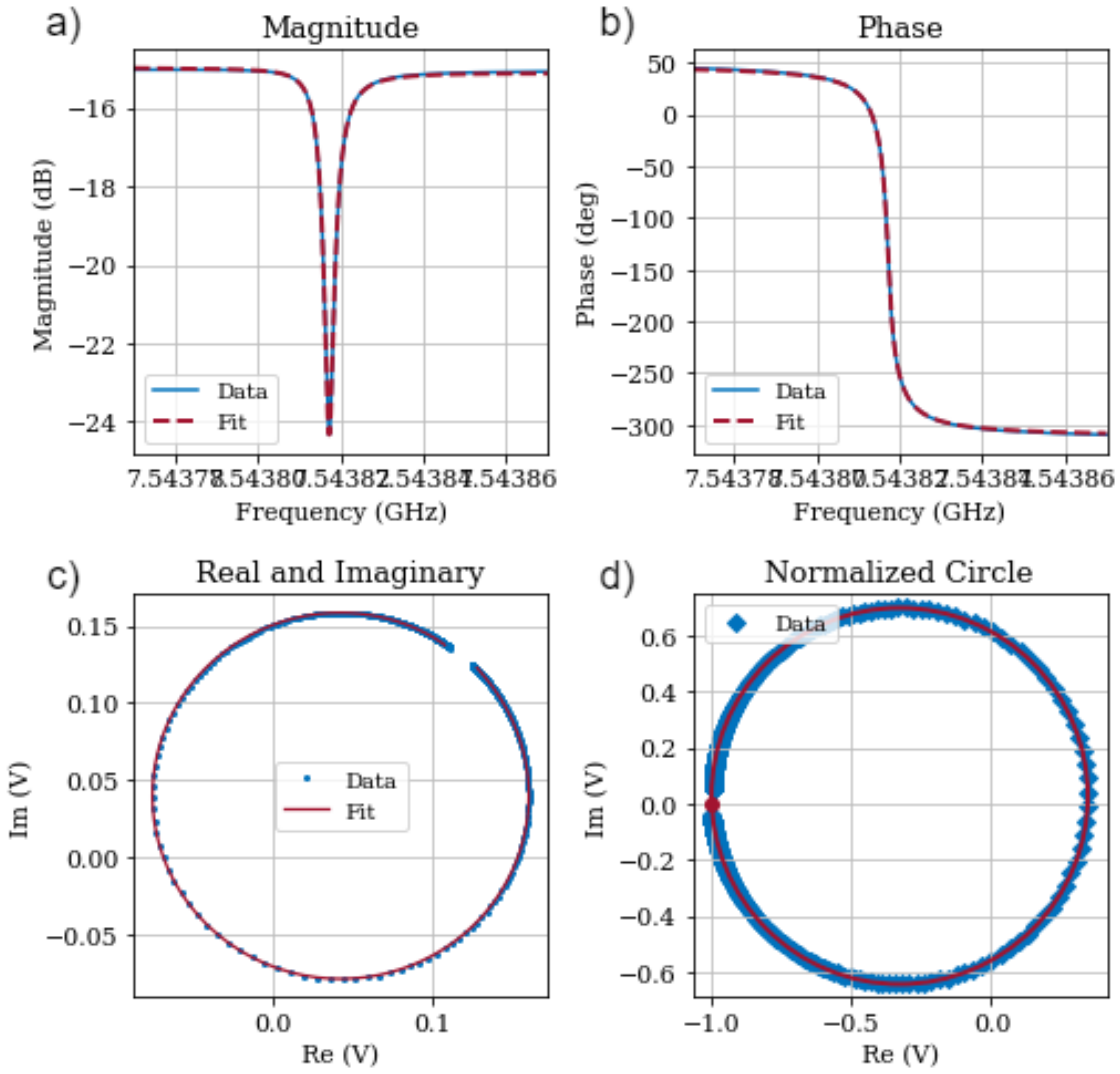

Figure 5.1: (a) Magnitude of the transmission signal. (b) Phase of the transmission signal. (c) Circle fit of the transmission signal. (d) Circle fit after compensating for external factors.

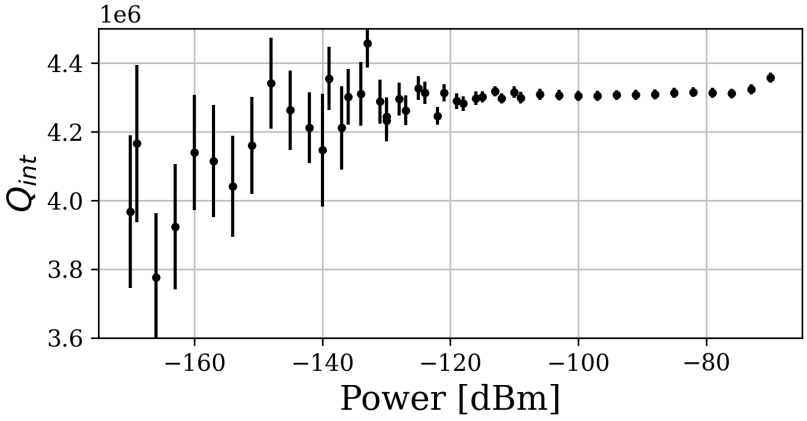

Figure 5.2: Power dependence of the internal quality factor of the niobium 3D-cavity. The x-axis shows the power at the sample. The quality factor seems consistent above approximately -120 dBm at approximately 4.3 million. At lower powers the uncertainty (standard deviation) of the circle fit increases significantly.

6
Conclusion

In continuous variable quantum computing, and quantum computing in general, thermal noise is a determining factor in how well our devices perform. With continuous variable quantum computing being a promising candidate for quantum information processing, this project aimed to characterize the thermal noise in a superconducting aluminum 3D-cavity coupled to a transmon qubit by measuring the thermal populations in the different parts of the system.

To do this, a couple different methods were used. The thermal excited population of the qubit was measured using e-f Rabi driving, following the scheme described in [3]. Measuring the qubit population after manually populating it and letting it decay, the resulting decay time measured deviated somewhat from the previously measured relaxation time of the qubit. This is likely due to the qubit not being allowed to decay freely before being read out. Other ways of validating this method could be attempted in future projects.

For measuring the thermal population of the 3D-cavity, two different methods were used. The first was based on Rabi driving while the second was based on Ramsey interferometry. With the same amount of data, taking roughly the same time, the Rabi driving method seemed to perform slightly better than the Ramsey interferometry in general while performing significantly better at low populations. While the favor seems to be with the Rabi driving method, the Ramsey method could potentially be improved significantly by introducing an echo pulse into the sequence, as in a T_2 echo measurement. An possible follow up to this thesis would be to test this. It could also be interesting to study the robustness of these methods against decoherence, detuning in the drive frequencies, residual population in higher energy levels of the qubit, etc.

The readout resonator thermal population couldn't be measured directly but an upper limit could be obtained by measuring the dephasing time of the qubit and assuming that the dephasing was purely caused by photon number fluctuations in the resonator. This gave a reasonable estimation on the order of the cavity and qubit populations.

The results of these four measurements are summarized in Table 6.1. All three components' effective temperatures are around 50 mk which is what we expect from our setup. Contrary to our expectation, however, the cavity is colder than the qubit. Due to its proximity to the cold environment we would expect the qubit to ther-

malize better than the cavity. While the readout resonator was expected to be the coldest, for the same reason, this could neither be confirmed nor denied with our estimation.

Our results compare well to previous studies such as J. M. Gertler et al. (2021) who measured a cavity population of 1-2% and a transmon population of 5% in a similar system [4], and R. W. Heeres et al. (2017) who measured a population of 2% in their cavity and 5% in their transmon [5]. X. Y. Yin et al. (2015) [30], who used the same method for measuring the transmon residual population, measured a population of 0.1 % corresponding to an effective temperature of 35 mK, which is somewhat lower than that of our system.

A subgoal of the project was to measure the quality factor of a niobium 3D-cavity. This was done with a circle fit as described in [6]. The measured quality factor of roughly four million aligns with what we expect for an unpolished cavity. The next step would be to polish the cavity to improve it further.

In summary, this project has demonstrated methods for characterizing the thermal populations and effective temperatures in different parts of a continuous variable quantum computing system, namely a qubit, 3D-cavity and readout resonator. These methods open up new possibilities to create larger experiments where the tools of measuring the effective temperatures could be used. For example, testing the effects of strong pump tones or Cooper pair-breaking radiation on the cavity temperature. Hopefully, the results of this thesis can support future research in circuit quantum electrodynamics and continuous variable quantum computing, by providing these simple ways of characterizing the thermal populations in circuit quantum electrodynamics platforms.

Table 6.1: Summary of the measured thermal populations in different parts of the sample. The errors are obtained with one standard deviation.

	Cavity		Qubit	Resonator
Method	Rabi	Ramsey	e-f Rabi	Dephasing
$\bar{n}_{th}$ [%]	0.34 ± 0.03	0.59 ± 0.013	0.25 ± 0.06	< 0.18
T_{eff} [mK]	37.6 ± 0.3	41.7 ± 1.9	50.2 ± 1.9	< 56.1

Bibliography

[1] A. Blais, A. L. Grimsmo, S. M. Girvin, and A. Wallraff, "Circuit quantum electrodynamics," *Rev. Mod. Phys.*, vol. 93, p. 025005, May 2021.

[2] L. Hu, Y. Ma, W. Cai, X. Mu, Y. Xu, W. Wang, Y. Wu, H. Wang, Y. P. Song, C.-L. Zou, and et al., "Quantum error correction and universal gate set operation on a binomial bosonic logical qubit," *Nature Physics*, vol. 15, p. 503–508, Feb 2019.

[3] K. Geerlings, Z. Leghtas, I. M. Pop, S. Shankar, L. Frunzio, R. J. Schoelkopf, M. Mirrahimi, and M. H. Devoret, "Demonstrating a driven reset protocol for a superconducting qubit," *Phys. Rev. Lett.*, vol. 110, p. 120501, Mar 2013.

[4] J. M. Gertler, B. Baker, J. Li, S. Shirol, J. Koch, and C. Wang, "Protecting a bosonic qubit with autonomous quantum error correction," *Nature*, vol. 590, pp. 243–248, feb 2021.

[5] R. W. Heeres, P. Reinhold, N. Ofek, L. Frunzio, L. Jiang, M. H. Devoret, and R. J. Schoelkopf, "Implementing a universal gate set on a logical qubit encoded in an oscillator," *Nature Communications*, vol. 8, jul 2017.

[6] S. Probst, F. B. Song, P. A. Bushev, A. V. Ustinov, and M. Weides, "Efficient and robust analysis of complex scattering data under noise in microwave resonators," *Review of Scientific Instruments*, vol. 86, no. 2, p. 024706, 2015.

[7] D. Deutsch and R. Jozsa, "Rapid solution of problems by quantum computation," *Proceedings of the Royal Society of London. Series A: Mathematical and Physical Sciences*, vol. 439, p. 553–558, Dec 1992.

[8] L. K. Grover, "A fast quantum mechanical algorithm for database search," *Proceedings of the twenty-eighth annual ACM symposium on Theory of computing - STOC '96*, Jul 1996.

[9] P. Shor, "Algorithms for quantum computation: discrete logarithms and factoring," in *Proceedings 35th Annual Symposium on Foundations of Computer Science*, pp. 124–134, 1994.

[10] R. P. Feynman, "Simulating physics with computers," *International Journal of Theoretical Physics*, vol. 21, pp. 467–488, jun 1982.

[11] A. Imamog¯lu, D. D. Awschalom, G. Burkard, D. P. DiVincenzo, D. Loss, M. Sherwin, and A. Small, "Quantum information processing using quantum dot spins and cavity qed," *Phys. Rev. Lett.*, vol. 83, pp. 4204–4207, Nov 1999.

[12] E. Knill, R. Laflamme, and G. J. Milburn, "A scheme for efficient quantum computation with linear optics," *Nature*, vol. 409, p. 46–52, Nov 2001.

[13] J. I. Cirac and P. Zoller, "Quantum computations with cold trapped ions," *Phys. Rev. Lett.*, vol. 74, pp. 4091–4094, May 1995.

[14] P. Krantz, M. Kjaergaard, F. Yan, T. P. Orlando, S. Gustavsson, and W. D. Oliver, "A quantum engineer's guide to superconducting qubits," *Applied Physics Reviews*, vol. 6, no. 2, p. 021318, 2019.

[15] M. Kudra, M. Kervinen, I. Strandberg, S. Ahmed, M. Scigliuzzo, A. Osman, D. P. Lozano, M. O. Tholén, R. Borgani, D. B. Haviland, G. Ferrini, J. Bylander, A. F. Kockum, F. Quijandría, P. Delsing, and S. Gasparinetti, "Robust preparation of wigner-negative states with optimized SNAP-displacement sequences," *PRX Quantum*, vol. 3, jul 2022.

[16] A. P. Sears, A. Petrenko, G. Catelani, L. Sun, H. Paik, G. Kirchmair, L. Frunzio, L. I. Glazman, S. M. Girvin, and R. J. Schoelkopf, "Photon shot noise dephasing in the strong-dispersive limit of circuit QED," *Physical Review B*, vol. 86, nov 2012.

[17] A. Romanenko, R. Pilipenko, S. Zorzetti, D. Frolov, M. Awida, S. Belomestnykh, S. Posen, and A. Grassellino, "Three-dimensional superconducting resonators at $T < 20$ mk with photon lifetimes up to $\tau = 2$ s," *Phys. Rev. Applied*, vol. 13, p. 034032, Mar 2020.

[18] M. Naghiloo, "Introduction to experimental quantum measurement with superconducting qubits," 2019.

[19] J. Johansson, P. Nation, and F. Nori, "Qutip: An open-source python framework for the dynamics of open quantum systems," *Computer Physics Communications*, vol. 183, no. 8, pp. 1760–1772, 2012.

[20] J. Johansson, P. Nation, and F. Nori, "Qutip 2: A python framework for the dynamics of open quantum systems," *Computer Physics Communications*, vol. 184, no. 4, pp. 1234–1240, 2013.

[21] B. Josephson, "Possible new effects in superconductive tunnelling," *Physics Letters*, vol. 1, no. 7, pp. 251–253, 1962.

[22] B. D. JOSEPHSON, "Coupled superconductors," *Rev. Mod. Phys.*, vol. 36, pp. 216–220, Jan 1964.

[23] C. Rigetti, J. M. Gambetta, S. Poletto, B. L. T. Plourde, J. M. Chow, A. D. Có rcoles, J. A. Smolin, S. T. Merkel, J. R. Rozen, G. A. Keefe, M. B. Rothwell, M. B. Ketchen, and M. Steffen, "Superconducting qubit in a waveguide cavity with a coherence time approaching 0.1 ms," *Physical Review B*, vol. 86, sep 2012.

[24] M. Pechal, *Microwave photonics in superconducting circuits*. PhD thesis, ETH Zurich, Zürich, 2016. Dissertation. ETH Zürich. 2016. No. 23835.

[25] H. Zu, W. Dai, and A. de Waele, "Development of dilution refrigerators—a review," *Cryogenics*, vol. 121, p. 103390, 2022.

[26] N. H. Balshaw, *Practical Cryogenics. An Introduction to Laboratory Cryogenics*. Oxford Instruments Superconductivity Limited, 1996.

[27] Intermodulation Products AB, "Synchronous microwave synthesis and analysis." `https://www.intermod.pro/products/microwave-platforms`. Accessed: 2022-12-13.

[28] Keysight, "Labber." `https://www.keysight.com/us/en/products/software/application-sw/labber-software.html`. Accessed: 2022-12-13.

[29] D. I. Schuster, A. A. Houck, J. A. Schreier, A. Wallraff, J. M. Gambetta, A. Blais, L. Frunzio, J. Majer, B. Johnson, M. H. Devoret, S. M. Girvin, and R. J. Schoelkopf, "Resolving photon number states in a superconducting circuit," *Nature*, vol. 445, pp. 515–518, feb 2007.

[30] X. Y. Jin, A. Kamal, A. P. Sears, T. Gudmundsen, D. Hover, J. Miloshi, R. Slattery, F. Yan, J. Yoder, T. P. Orlando, S. Gustavsson, and W. D. Oliver, "Thermal and residual excited-state population in a 3d transmon qubit," *Phys. Rev. Lett.*, vol. 114, p. 240501, Jun 2015.

[31] D. C. Brody and L. P. Hughston, "The quantum canonical ensemble," *Journal of Mathematical Physics*, vol. 39, pp. 6502–6508, dec 1998.

A

Supplementary Calculations

A.1 Derivations of Distributions of Thermal Excitations

In this appendix I derive the distributions of thermal excitations in a quantum system and more specifically, in the two systems we are interested in for this thesis: the transmon qubit and the quantum harmonic oscillator.

The density matrix of a state in thermal equilibrium with an environment at temperature T can be written as [31]

$$\rho_{th} = \frac{1}{Z} e^{-\frac{H}{k_B T}}, \tag{A.1a}$$

$$Z = \mathrm{Tr}\left[e^{-\frac{H}{k_B T}} \right], \tag{A.1b}$$

where H is the Hamiltonian of the system, k_B is Boltzmann's constant and Z is the partition function. For an arbitrary N-dimensional Hamiltonian $H = \sum_{n=0}^{N} E_n \left|n\right\rangle \left\langle n\right|$ with eigenenergies E_n we can calculate the partition function as

$$Z = \sum_{n=0}^{N} e^{-\frac{E_n}{k_B T}}. \tag{A.2}$$

The probability that the system is in Fock state $\left|n\right\rangle$ is then

$$P_n = \left\langle n\right| \rho_{th} \left|n\right\rangle. \tag{A.3}$$

By plugging in equation (A.1) and (A.2) we get

$$\begin{aligned} P_n &= \left\langle n\right| \rho_{th} \left|n\right\rangle, \\ &= \left\langle n\right| \frac{1}{Z} e^{-H/k_B T} \left|n\right\rangle, \\ &= \frac{1}{Z} e^{-E_n/k_B T} \left\langle n|n\right\rangle, \\ &= \frac{e^{-E_n/k_B T}}{\sum_{n=0}^{N} e^{-E_n/k_B T}}. \end{aligned} \tag{A.4}$$

We can now use this general expression to find the distributions in thermal equilibrium of some systems that will be of interest to us. One of the simplest cases is a

two-level system with energy spacing $E_{|e\rangle} - E_{|g\rangle} = \hbar\omega$ which has the distribution

$$P_{|g\rangle} = \frac{1}{1 + e^{-\hbar\omega/k_B T}}, \quad P_{|e\rangle} = \frac{e^{-\hbar\omega/k_B T}}{1 + e^{-\hbar\omega/k_B T}}, \tag{A.5}$$

where $|g\rangle$ and $|e\rangle$ indicates the ground state and the excited state.

For a transmon with the Hamiltonian and eigenenergies seen in equation (2.18) and (2.19) we get the distribution

$$P_n = \frac{e^{-(\hbar\omega n - \frac{E_C}{2}(n-1)n)/k_B T}}{\sum_{m=0}^{\infty} e^{-(\hbar\omega n - \frac{E_C}{2}(n-1)n)/k_B T}}. \tag{A.6}$$

We can write the distributions for the first three energy leves, which we denote with $|g\rangle$, $|e\rangle$ and $|f\rangle$, as

$$P_{|g\rangle} = \frac{1}{1 + e^{-\hbar\omega/k_B T} + e^{-(2\hbar\omega - E_C)/k_B T} + ...}, \tag{A.7a}$$

$$P_{|e\rangle} = \frac{e^{-\hbar\omega/k_B T}}{1 + e^{-\hbar\omega/k_B T} + e^{-(2\hbar\omega - E_C)/k_B T} + ...}, \tag{A.7b}$$

$$P_{|f\rangle} = \frac{e^{-(2\hbar\omega - E_C)/k_B T}}{1 + e^{-\hbar\omega/k_B T} + e^{-(2\hbar\omega - E_C)/k_B T} + ...}. \tag{A.7c}$$

Lastly, we look at the quantum harmonic oscillator with the Hamiltonian and eigenenergies seen in equation (2.4) and (2.5). For this system we can reuse the previous calculations by setting $E_C = 0$. We then get

$$P_n = \frac{e^{-\hbar\omega n/k_B T}}{\sum_{m=0}^{\infty} e^{-\hbar\omega n/k_B T}}. \tag{A.8}$$

Note that the additional factors $e^{-\hbar\omega/2k_B T}$ in the numerator and denominator from the harmonic oscillator hamiltonian cancel each other out. This expression can be simplified further by explicitly calculating the infinite sum.

$$\begin{aligned} P_n &= \frac{e^{-\hbar\omega n/k_B T}}{\sum_{m=0}^{\infty} e^{-\hbar\omega n/k_B T}} \\ &= \frac{e^{\hbar\omega/k_B T} - 1}{e^{\hbar\omega/k_B T}} e^{-\hbar\omega n/k_B T}. \end{aligned} \tag{A.9}$$

Additionally, we may calculate the average photon number in the harmonic oscillator as

$$\begin{aligned} \bar{n} &= \sum_{n=0}^{\infty} n P_n \\ &= \frac{e^{-\hbar\omega/k_B T}}{1 - e^{-\hbar\omega/k_B T}}, \end{aligned} \tag{A.10}$$

where we have used that $\sum_{n=0}^{\infty} n x^n = x/(x-1)^2$. Rearanging this we get

$$e^{-\hbar\omega/k_B T} = \frac{\bar{n}}{\bar{n} + 1}, \tag{A.11}$$

which we can use to express the probability P_n in terms of $\bar{n}$. We see that the probability is

$$\begin{aligned} P_n &= (1 - \frac{\bar{n}}{\bar{n}+1})(\frac{\bar{n}}{\bar{n}+1})^n \\ &= \frac{\bar{n}^n}{(\bar{n}+1)^{n+1}}. \end{aligned} \tag{A.12}$$

A.2 Derivations of Driving the Qubit

In this appendix I derive the time evolution of a driven qubit. As stated in section 2.4, in a rotating frame a driven qubit has the Hamiltonian

$$\tilde{H}/\hbar = -\frac{\Delta_d}{2}\hat{\sigma}_z - \frac{A}{2}\hat{\sigma}_x, \tag{A.13}$$

with $\Delta_d = \omega_q - \omega_d$. The eigenvalues are

$$E_\pm = \pm\frac{\hbar}{2}\sqrt{A^2 + \Delta_d^2}, \tag{A.14}$$

and the eigenstates

$$|V_+\rangle = \cos\theta\,|e\rangle - \sin\theta\,|g\rangle\,, \tag{A.15a}$$
$$|V_-\rangle = \sin\theta\,|e\rangle + \cos\theta\,|g\rangle\,, \tag{A.15b}$$

where $\theta = \tan^{-1}\left(\frac{A}{\sqrt{A^2+\Delta_d^2}-\Delta_d}\right)$ [18]. An arbitrary state written in this eigenbasis evolves as

$$|\psi(t)\rangle = C_+ e^{-iE_+ t}\,|V_+\rangle + C_- e^{-iE_- t}\,|V_-\rangle\,, \tag{A.16}$$

where the coefficients $C_\pm$ relate to the initial state of the qubit, $|\psi(0)\rangle = \alpha\,|g\rangle + \beta\,|e\rangle$, as

$$C_+ = \beta\sin\theta + \alpha\cos\theta, \tag{A.17a}$$
$$C_- = \beta\cos\theta - \alpha\sin\theta. \tag{A.17b}$$

Plugging in equation (A.15) and (A.17) into (A.16) we get

$$\begin{aligned} |\psi(t)\rangle =& \left[C_+ e^{-iE_+ t}\sin\theta + C_- e^{-iE_- t}\cos\theta\right]|e\rangle \\ &+ \left[C_+ e^{-iE_+ t}\cos\theta - C_- e^{-iE_- t}\sin\theta\right]|g\rangle = \\ =& \Bigg[\left(\beta\frac{1-\cos(2\theta)}{2} + \alpha\frac{\sin(2\theta)}{2}\right)e^{-iE_+ t} \\ &+ \left(\beta\frac{1+\cos(2\theta)}{2} - \alpha\frac{\sin(2\theta)}{2}\right)e^{-iE_- t}\Bigg]|e\rangle \\ &+ \Bigg[\left(\beta\frac{\sin(2\theta)}{2} + \alpha\frac{1+\cos(2\theta)}{2}\right)e^{-iE_+ t} \\ &- \left(\beta\frac{\sin(2\theta)}{2} - \alpha\frac{1-\cos(2\theta)}{2}\right)e^{-iE_- t}\Bigg]|g\rangle\,. \end{aligned} \tag{A.18}$$

Rearranging terms we can write this as

$$\begin{aligned}|\psi(t)\rangle = \Bigg[&\beta\frac{1}{2}\left(e^{-iE_+t}+e^{-iE_-t}\right)+\beta\frac{\cos(2\theta)}{2}\left(-e^{-iE_+t}+e^{-iE_-t}\right)\\ &+\alpha\frac{\sin(2\theta)}{2}\left(e^{-iE_+t}-e^{-iE_-t}\right)\Bigg]|e\rangle\\ +\Bigg[&\alpha\frac{1}{2}\left(e^{-iE_+t}+e^{-iE_-t}\right)+\beta\frac{\sin(2\theta)}{2}\left(e^{-iE_+t}-e^{-iE_-t}\right)\\ &+\alpha\frac{\cos(2\theta)}{2}\left(e^{-iE_+t}-e^{-iE_-t}\right)\Bigg]|g\rangle\,. \end{aligned} \tag{A.19}$$

Then, identifying the exponential forms of the sine and cosine functions, we can finally rewrite this without the exponential terms.

$$\begin{aligned}|\psi(t)\rangle = &\left[\beta\cos\left(\frac{\Omega_R}{2}t\right)+i\Big(\beta\cos(2\theta)-\alpha\sin(2\theta)\Big)\sin\left(\frac{\Omega_R}{2}t\right)\right]|e\rangle\\ +&\left[\alpha\cos\left(\frac{\Omega_R}{2}t\right)-i\Big(\beta\sin(2\theta)+\alpha\cos(2\theta)\Big)\sin\left(\frac{\Omega_R}{2}t\right)\right]|g\rangle\,, \end{aligned} \tag{A.20}$$

where we have also defined the Rabi frequency $\Omega_R = \sqrt{A^2+\Delta_d^2}$. This expression describes how an arbitrary qubit state evolves under a coherent drive. For initial state $|\psi(0)\rangle = |g\rangle$ this becomes

$$\begin{aligned}|\psi(t)\rangle = &-i\sin(2\theta)\sin\left(\frac{\Omega_R}{2}t\right)|e\rangle\\ &+\left(\cos\left(\frac{\Omega_R}{2}t\right)-i\cos(2\theta)\sin\left(\frac{\Omega_R}{2}t\right)\right)|g\rangle\,, \end{aligned} \tag{A.21}$$

from which we can calculate the time-dependent excited population,

$$P_{|e\rangle} = \frac{A^2}{\Omega_R^2}\sin^2\left(\frac{\Omega_R}{2}t\right), \tag{A.22}$$

where we have used that $\sin^2(2\theta) = A^2/\Omega_R^2$ [18].

A.3 Calculations for Measuring Cavity Thermal Population using Rabi Driving

In this appendix I derive the results of the measurement of thermal population in a cavity using Rabi driving (as described in Section 4.2.1), and show that the result is independent of the excited population in the coupled qubit. We will find that the excited population of the qubit only affects the contrast of the measurement.

We will start with an initial state

$$|\psi_i\rangle = \left(\sqrt{1-\epsilon}\,|g\rangle+\sqrt{\epsilon}\,|e\rangle\right)\left(\sqrt{1-\delta}\,|0\rangle+\sqrt{\delta}\,|1\rangle\right), \tag{A.23}$$

where $\epsilon, \delta \ll 1$ are the first excited populations of the qubit and cavity, respectively. The goal will then be to find δ. We assume here that the populations of higher energy states are negligible.

The Rabi driving of the qubit can be described using the unitary rotation operator $R_x(\Omega)$ which acts on an arbitrary state $|\psi\rangle = \alpha|g\rangle + \beta|e\rangle$ as

$$R_x(\theta)|\psi\rangle = \left(\alpha\cos\frac{\theta}{2} - i\beta\sin\frac{\theta}{2}\right)|g\rangle + \left(-i\alpha\sin\frac{\theta}{2} + \beta\cos\frac{\theta}{2}\right)|e\rangle\,. \tag{A.24}$$

Note that this is the same state as seen in equation (A.20) when $\Delta_d = 0$ (and the notation is changed from $\Omega_R t$ to θ). We will assume that this operation is perfectly selective on the states of the cavity and indicate the state it is conditional on with a superscript, as $R_x^{|0\rangle}(\theta)$ and $R_x^{|1\rangle}(\theta)$.

Now, let us apply the rotation operator, selective on $|0\rangle$, on our initial state. This gives us

$$\begin{aligned}
R_x^{|0\rangle}(\theta)|\psi_i\rangle &= R_x^{|0\rangle}(\theta)\left(\sqrt{1-\epsilon}\,|g\rangle + \sqrt{\epsilon}\,|e\rangle\right)\left(\sqrt{1-\delta}\,|0\rangle + \sqrt{\delta}\,|1\rangle\right) \\
&= \mathrm{R}_x(\theta)\left(\sqrt{1-\epsilon}\,|g\rangle + \sqrt{\epsilon}\,|e\rangle\right)\sqrt{1-\delta}\,|0\rangle \\
&+ \left(\sqrt{1-\epsilon}\,|g\rangle + \sqrt{\epsilon}\,|e\rangle\right)\sqrt{\delta}\,|1\rangle \\
&= \left[\left(\sqrt{1-\epsilon}\cos\frac{\theta}{2} - i\sqrt{\epsilon}\sin\frac{\theta}{2}\right)|g\rangle\right. \\
&+ \left.\left(-i\sqrt{1-\epsilon}\sin\frac{\theta}{2} + \sqrt{\epsilon}\cos\frac{\theta}{2}\right)|e\rangle\right]\sqrt{1-\delta}\,|0\rangle \\
&+ \left(\sqrt{1-\epsilon}\,|g\rangle + \sqrt{\epsilon}\,|e\rangle\right)\sqrt{\delta}\,|1\rangle \\
&= \left[\left(\sqrt{1-\epsilon}\cos\frac{\theta}{2} - i\sqrt{\epsilon}\sin\frac{\theta}{2}\right)\sqrt{1-\delta}\,|0\rangle\right. \\
&\quad \left. + \sqrt{1-\epsilon}\sqrt{\delta}\,|1\rangle\right]|g\rangle \\
&+ \left[\left(-i\sqrt{1-\epsilon}\sin\frac{\theta}{2} + \sqrt{\epsilon}\cos\frac{\theta}{2}\right)\sqrt{1-\delta}\,|0\rangle\right. \\
&\quad \left. + \sqrt{\epsilon}\sqrt{\delta}\,|1\rangle\right]|e\rangle \qquad \text{(A.25)} \\
&\equiv |\psi_f\rangle\,. \qquad \text{(A.26)}
\end{aligned}$$

We can now calculate the population of the first excited state of the qubit after the

Rabi driving as

$$\begin{aligned} P_{|e\rangle}^{|0\rangle} &= \langle\psi_f|e\rangle\langle e|\psi_f\rangle \\ &= \left|\left(-i\sqrt{1-\epsilon}\sin\frac{\theta}{2}+\sqrt{\epsilon}\cos\frac{\theta}{2}\right)\sqrt{1-\delta}\right|^2+\left|\sqrt{\epsilon}\sqrt{\delta}\right|^2 \\ &= \left|\sqrt{1-\epsilon}\sqrt{1-\delta}\sin\frac{\theta}{2}\right|^2+\left|\sqrt{\epsilon}\sqrt{1-\delta}\cos\frac{\theta}{2}\right|^2+\left|\sqrt{\epsilon}\sqrt{\delta}\right|^2 \\ &= (1-\epsilon)(1-\delta)\sin^2\frac{\theta}{2}+\epsilon(1-\delta)\cos^2\frac{\theta}{2}+\epsilon\delta \\ &= (1-\delta)\left[\frac{1}{2}+\left(\epsilon-\frac{1}{2}\cos\theta\right)\right]+\epsilon\delta, \end{aligned} \tag{A.27}$$

where the addition formula for cosine was used in the last equality. This expression oscillates with an amplitude $A_0 = \frac{1}{2}(1-\delta)(2\epsilon-1)$.

We can now perform the same calculation with a rotation selective on $|1\rangle$. We then get

$$\begin{aligned} R_x^{|1\rangle}(\theta)|\psi_i\rangle = &\left[\sqrt{1-\epsilon}\sqrt{1-\delta}|0\rangle\right. \\ &\left.+\left(\sqrt{1-\epsilon}\cos\frac{\theta}{2}-i\sqrt{\epsilon}\sin\frac{\theta}{2}\right)\sqrt{\delta}|1\rangle\right]|g\rangle \\ &+\left[\sqrt{\epsilon}\sqrt{1-\delta}|0\rangle\right. \\ &\left.+\left(-i\sqrt{1-\epsilon}\sin\frac{\theta}{2}+\sqrt{\epsilon}\cos\frac{\theta}{2}\right)\sqrt{\delta}|1\rangle\right]|e\rangle. \end{aligned} \tag{A.28}$$

From this we can calculate the population in the excited state of the qubit in the same way as above and get

$$P_{|e\rangle}^{|1\rangle} = \epsilon\big(1-\delta\big)+\delta\left[\frac{1}{2}+\left(\epsilon-\frac{1}{2}\cos\theta\right)\right], \tag{A.29}$$

which oscillates with an amplitude $A_1 = \frac{1}{2}\delta(2\epsilon-1)$.

We can now take the ratio of these two amplitudes to get the population of the in the first excited state of the cavity, δ, as

$$\begin{aligned} \frac{A_1}{A_0} &= \frac{\frac{1}{2}\delta(2\epsilon-1)}{\frac{1}{2}(1-\delta)(2\epsilon-1)} \\ &= \frac{\delta}{1-\delta}. \end{aligned} \tag{A.30}$$

We see that this does not depend on the population of the of the first excited state of the qubit, ϵ. Thus, under the assumption that the populations in higher energy states of the cavity and the qubit are negligible and that our Rabi driving is perfectly selective, the population in the qubit doesn't change the result of the measurement. It only reduces the contrast, making it more sensitive to noise.

A.4 Calculations for Measuring Cavity Thermal Population using Ramsey Driving

In this appendix I derive the results of the measurement of thermal population in a cavity using Ramsey interferometry (as described in Section 4.2.2), and show that the result is independent of the excited population in the coupled qubit. As for the measurement using Rabi driving, we will find that the excited population of the qubit only affects the contrast of the measurement. We will start with the same initial state as in that case, described in equation (A.23).

Furthermore, we will utilize the rotation operator described in equation (A.24). However, the rotation will now be unconditional on the state of the cavity. for an angle $\theta = \frac{\pi}{2}$ this operator acts on an arbitrary state $|\psi\rangle = \alpha|g\rangle + \beta|e\rangle$ as

$$R_x(\pi/2)|\psi\rangle = \frac{\alpha - i\beta}{\sqrt{2}}|e\rangle + \frac{-i\alpha + \beta}{\sqrt{2}}|e\rangle . \tag{A.31}$$

The free evolution of the qubit state can be described by the unitary operator $U = e^{i\frac{\omega_q}{2}\hat{\sigma}_z t}$ which takes an arbitrary state $|\psi\rangle$ to

$$U|\psi\rangle = \alpha e^{i\omega_q t/2}|g\rangle + \beta e^{-i\omega_q t/2}|e\rangle , \tag{A.32}$$

where ω_q is the qubit frequency and t is the duration of the free evolution. We will also use that the qubit frequency depends on the state of the cavity, as described in equation (2.36). Thus, this operator will be conditional on the state of the cavity.

The qubit state after the full Ramsey sequence will be

$$\begin{aligned}
&R_x(\pi/2)UR_x(\pi/2)|\psi_i\rangle = \\
&= R_x(\pi/2)UR_x(\pi/2)\left(\sqrt{1-\epsilon}|g\rangle + \sqrt{\epsilon}|e\rangle\right)\left(\sqrt{1-\delta}|0\rangle + \sqrt{\delta}|1\rangle\right) \\
&= R_x(\pi/2)U\left(\frac{\sqrt{1-\epsilon}-i\sqrt{\epsilon}}{\sqrt{2}}|g\rangle + \frac{\sqrt{\epsilon}-i\sqrt{1-\epsilon}}{\sqrt{2}}|e\rangle\right)\left(\sqrt{1-\delta}|0\rangle + \sqrt{\delta}|1\rangle\right) \\
&= R_x(\pi/2)\Bigg[\left(\frac{\sqrt{1-\epsilon}-i\sqrt{\epsilon}}{\sqrt{2}}e^{i\omega_q t/2}|g\rangle + \frac{\sqrt{\epsilon}-i\sqrt{1-\epsilon}}{\sqrt{2}}e^{-i\omega_q t/2}|e\rangle\right)\sqrt{1-\delta}|0\rangle \\
&\quad + \left(\frac{\sqrt{1-\epsilon}-i\sqrt{\epsilon}}{\sqrt{2}}e^{i(\omega_q+2\chi)t/2}|g\rangle + \frac{\sqrt{\epsilon}-i\sqrt{1-\epsilon}}{\sqrt{2}}e^{-i(\omega_q+2\chi)t/2}|e\rangle\right)\sqrt{\delta}|1\rangle\Bigg] \\
&= \Bigg[\frac{1}{\sqrt{2}}\left(\frac{\sqrt{1-\epsilon}-i\sqrt{\epsilon}}{\sqrt{2}}e^{i\omega_q t/2} - i\frac{\sqrt{\epsilon}-i\sqrt{1-\epsilon}}{\sqrt{2}}e^{-i\omega_q t/2}\right)|g\rangle \\
&\quad + \frac{1}{\sqrt{2}}\left(\frac{\sqrt{\epsilon}-i\sqrt{1-\epsilon}}{\sqrt{2}}e^{i\omega_q t/2} - i\frac{\sqrt{1-\epsilon}-i\sqrt{\epsilon}}{\sqrt{2}}e^{-i\omega_q t/2}\right)|e\rangle\Bigg]\sqrt{1-\delta}|0\rangle \\
&+ \Bigg[\frac{1}{\sqrt{2}}\left(\frac{\sqrt{1-\epsilon}-i\sqrt{\epsilon}}{\sqrt{2}}e^{i(\omega_q+2\chi)t/2} - i\frac{\sqrt{\epsilon}-i\sqrt{1-\epsilon}}{\sqrt{2}}e^{-i(\omega_q+2\chi)t/2}\right)|g\rangle \\
&\quad + \frac{1}{\sqrt{2}}\left(\frac{\sqrt{\epsilon}-i\sqrt{1-\epsilon}}{\sqrt{2}}e^{i(\omega_q+2\chi)t/2} - i\frac{\sqrt{1-\epsilon}-i\sqrt{\epsilon}}{\sqrt{2}}e^{-i(\omega_q+2\chi)t/2}\right)|e\rangle\Bigg]\sqrt{\delta}|1\rangle .
\end{aligned} \tag{A.33}$$

Rearranging the terms somewhat, this becomes

$$
\begin{aligned}
&R_x(\pi/2)UR_x(\pi/2)\,|\psi_i\rangle = \\
&= \left[\frac{1}{\sqrt{2}}\left(\frac{\sqrt{1-\epsilon}-i\sqrt{\epsilon}}{\sqrt{2}}e^{i\omega_q t/2} - i\frac{\sqrt{\epsilon}-i\sqrt{1-\epsilon}}{\sqrt{2}}e^{-i\omega_q t/2}\right)\sqrt{1-\delta}\,|0\rangle\right. \\
&\quad \left. + \frac{1}{\sqrt{2}}\left(\frac{\sqrt{1-\epsilon}-i\sqrt{\epsilon}}{\sqrt{2}}e^{i(\omega_q+2\chi)t/2} - i\frac{\sqrt{\epsilon}-i\sqrt{1-\epsilon}}{\sqrt{2}}e^{-i(\omega_q+2\chi)t/2}\right)\sqrt{\delta}\,|1\rangle\right]|g\rangle \\
&+ \left[\frac{1}{\sqrt{2}}\left(\frac{\sqrt{\epsilon}-i\sqrt{1-\epsilon}}{\sqrt{2}}e^{i\omega_q t/2} - i\frac{\sqrt{1-\epsilon}-i\sqrt{\epsilon}}{\sqrt{2}}e^{-i\omega_q t/2}\right)\sqrt{1-\delta}\,|0\rangle\right. \\
&\quad \left. + \frac{1}{\sqrt{2}}\left(\frac{\sqrt{\epsilon}-i\sqrt{1-\epsilon}}{\sqrt{2}}e^{i(\omega_q+2\chi)t/2} - i\frac{\sqrt{1-\epsilon}-i\sqrt{\epsilon}}{\sqrt{2}}e^{-i(\omega_q+2\chi)t/2}\right)\sqrt{\delta}\,|1\rangle\right]|e\rangle \\
&\equiv |\psi_f\rangle\,. \qquad \text{(A.34)}
\end{aligned}
$$

Now, let us look at only the term of the excited qubit state since that's the one we are interested in measuring (and because these calculations are quite tedious). We can simplify this expression as

$$
\begin{aligned}
&\left[\frac{1}{\sqrt{2}}\left(\frac{\sqrt{\epsilon}-i\sqrt{1-\epsilon}}{\sqrt{2}}e^{i\omega_q t/2} - i\frac{\sqrt{1-\epsilon}-i\sqrt{\epsilon}}{\sqrt{2}}e^{-i\omega_q t/2}\right)\sqrt{1-\delta}\,|0\rangle\right. \\
&\quad \left. + \frac{1}{\sqrt{2}}\left(\frac{\sqrt{\epsilon}-i\sqrt{1-\epsilon}}{\sqrt{2}}e^{i(\omega_q+2\chi)t/2} - i\frac{\sqrt{1-\epsilon}-i\sqrt{\epsilon}}{\sqrt{2}}e^{-i(\omega_q+2\chi)t/2}\right)\sqrt{\delta}\,|1\rangle\right]|e\rangle \\
&= \left[\left(\sqrt{\epsilon}\frac{e^{i\omega_q t/2}-e^{-i\omega_q t/2}}{2} - i\sqrt{1-\epsilon}\frac{e^{i\omega_q t/2}+e^{-i\omega_q t/2}}{2}\right)\sqrt{1-\delta}\,|0\rangle\right. \\
&\quad \left. + \left(\sqrt{\epsilon}\frac{e^{i(\omega_q+2\chi)t/2}-e^{-i(\omega_q+2\chi)t/2}}{2} - i\sqrt{1-\epsilon}\frac{e^{i(\omega_q+2\chi)t/2}+e^{-i(\omega_q+2\chi)t/2}}{2}\right)\sqrt{\delta}\,|1\rangle\right]|e\rangle \\
&= \left[\left(i\sqrt{\epsilon}\sin\frac{\omega_q t}{2} - i\sqrt{1-\epsilon}\cos\frac{\omega_q t}{2}\right)\sqrt{1-\delta}\,|0\rangle\right. \\
&\quad \left. + \left(i\sqrt{\epsilon}\sin\frac{(\omega_q+2\chi)t}{2} - i\sqrt{1-\epsilon}\cos\frac{(\omega_q+2\chi)t}{2}\right)\sqrt{\delta}\,|1\rangle\right]|e\rangle\,, \qquad \text{(A.35)}
\end{aligned}
$$

where we used the exponential forms of sine and cosine in the last equality. We can finally calculate the population in the excited state of the qubit after the Ramsey sequence as

$$
\begin{aligned}
P_{|e\rangle} &= \langle\psi_f|e\rangle\,\langle e|\psi_f\rangle \\
&= \left|\left(i\sqrt{\epsilon}\sin\frac{\omega_q t}{2} - i\sqrt{1-\epsilon}\cos\frac{\omega_q t}{2}\right)\sqrt{1-\delta}\right|^2 \\
&\quad + \left|i\sqrt{\epsilon}\sin\frac{(\omega_q+2\chi)t}{2} - i\sqrt{1-\epsilon}\cos\frac{(\omega_q+2\chi)t}{2}\right)\sqrt{\delta}\right|^2 \\
&= (1-\delta)\left(\frac{1}{2} + \frac{1-2\epsilon}{2}\cos\omega_q t - \sqrt{\epsilon}\sqrt{1-\epsilon}\sin\omega_q t\right) \\
&\quad + \delta\left(\frac{1}{2} + \frac{1-2\epsilon}{2}\cos\Big((\omega_q+2\chi)t\Big) - \sqrt{\epsilon}\sqrt{1-\epsilon}\sin\Big((\omega_q+2\chi)t\Big)\right) \\
&= (1-\delta)\left(\frac{1}{2} + R\cos(\omega_q t+\phi)\right) + \delta\left(\frac{1}{2} + R\cos\Big((\omega_q+2\chi)t+\phi\Big)\right), \qquad \text{(A.36)}
\end{aligned}
$$

where $R = \frac{1}{2}\sqrt{(1-2\epsilon)^2 + \epsilon(1-\epsilon)}$ and $\tan\phi = \sqrt{\epsilon}\sqrt{1-\epsilon}/(1-2\epsilon)$. The last two equalities where again obtained by using the addition formulas for sine and cosine.

We see that the population consists of two oscillating terms at frequencies ω_q and $\omega_q + 2\chi$ with amplitudes $A_0 = (1-\delta)R$ and $A_1 = \delta R$, respectively. Comparing the amplitude of each oscillation, we get

$$\begin{aligned} \frac{A_1}{A_0} &= \frac{\delta R}{(1-\delta)R} \\ &= \frac{\delta}{1-\delta}, \end{aligned} \tag{A.37}$$

from which we can extract the excited population of the cavity, δ. We once again find that this does not depend on the population of the first excited state of the qubit, ϵ. Thus, the population in the qubit doesn't change the result of the measurement, only the contrast, as we saw for the Rabi driving measurement as well. Note that we also disregarded the decay of the excited state during the free evolution. While the decay of the cavity is slow enough that we can neglect it, the decay of the qubit is not. Rather, the qubit can decay significantly during the measurement. However, since the decay doesn't depend on the state of the cavity, it won't affect the outcome of the measurement (essentially, it will cancel out when we take the ratio in equation (A.37)).

DEPARTMENT OF MICROTECHNOLOGY AND NANOSCIENCE
CHALMERS UNIVERSITY OF TECHNOLOGY
Gothenburg, Sweden
www.chalmers.se

CHALMERS
UNIVERSITY OF TECHNOLOGY